# Redox Kinetics Study of Fuel Reduced Ceria for Chemical-Looping Water Splitting

Zhenlong Zhao,[†] Mruthunjaya Uddi,[§] Nikolai Tsvetkov,[‡] Bilge Yildiz,*[,‡] and Ahmed F. Ghoniem*[,†]

[†]Department of Mechanical Engineering and [‡]Department of Nuclear Science & Engineering, Massachusetts Institute of Technology, 77 Massachusetts Avenue, Cambridge, Massachusetts 02139-4307, United States

[§]Department of Mechanical Engineering, University of Alabama, Tuscaloosa, Alabama 35487, United States

ABSTRACT: Chemical-looping water splitting is a novel and promising technology for hydrogen production with CO_2 separation. Its efficiency and performance depend critically on the reduction and oxidation (redox) properties of the oxygen carriers (OC). Ceria is recognized as one of the most promising OC candidates, because of its fast chemistry, high ionic diffusivity, and large oxygen storage capacity. The fundamental surface redox pathways, including the complex interactions of mobile ions and electrons between the bulk and the surface, along with the adsorbates and electrostatic fields, remain yet unresolved. This work presents a detailed redox kinetics study with emphasis on the surface ion-incorporation kinetics pathway, using time-resolved and systematic measurements in the temperature range 600−1000 °C. By using fine ceria nanopowder, we observe an order-of-magnitude higher hydrogen production rate compared to the state-of-the-art thermochemical or reactive chemical-looping water splitting studies. We show that the reduction is the rate-limiting step, and it determines the total amount of hydrogen produced in the following oxidation step. The redox kinetics is modeled using a two-step surface chemistry (an H_2O adsorption/dissociation step and a charge-transfer step), coupled with the bulk-to-surface transport equilibrium. Kinetics and equilibrium parameters are extracted with excellent agreement with measurements. The model reveals that the surface defects are abundant during redox conditions, and charge transfer is the rate-determining step for H_2 production. The results establish a baseline for developing new materials and provide guidance for the design and the practical application of water splitting technology (e.g., the design of OC characteristics, the choice of the operating temperatures, and periods for redox steps, etc.). The method, combining well-controlled experiment and detailed kinetics modeling, enables a new and thorough approach for examining the defect thermodynamics in the bulk and at the surface, as well as redox reaction kinetics for alternative materials for water splitting.
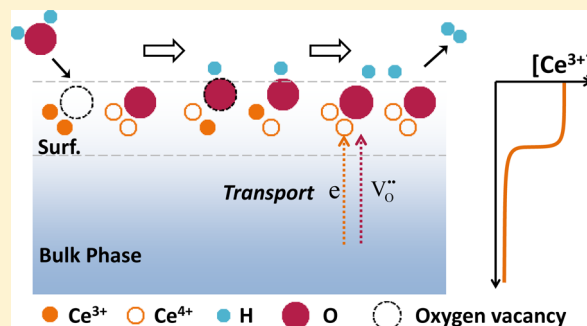
1. INTRODUCTION

Hydrogen is an important environmentally friendly energy carrier because of its high gravimetric energy density and zero emission. Moreover, hydrogen finds wide applications in a variety of industries, including crude oil refining, chemical production, aerospace, metal refining, food processing, and electronics manufacturing. Currently, steam methane reforming (SMR) is the major hydrogen production method. However, SMR leads to significant greenhouse gas emission, and it has already reached its maximum efficiency (70−85%).[1] The growing demand for clean and cost-efficient hydrogen sources has led to significant efforts to develop alternative technologies.[2,3]

Among a variety of options, thermochemical water splitting (TCWS) has recently attracted significant attention, because of its potential for high conversion efficiencies with limited emissions.[4,5] This approach is based on a two-step mechanism using a metal oxide (such as ceria-based materials) to dissociate H_2O into H_2 and heat to reduce the metal oxide:

endothermic reduction step:

$$Me_xO_y \rightarrow Me_xO_{y-1} + \tfrac{1}{2}O_2 \qquad (1)$$
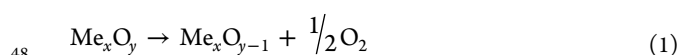
exothermic oxidation step:

$$H_2O + Me_xO_{y-1} \rightarrow H_2 + Me_xO_y \qquad (2)$$

The reduction step proceeds at higher temperature (above 1400 °C) to form oxygen vacancies and release O_2, while the oxidation step takes place at lower temperature (below 1000 °C) to dissociate H_2O and generate H_2. During this process, the metal oxide transports oxygen between the two steps, remaining intact at the end of the cycle. As such, it is commonly referred to as the "oxygen carrier (OC)". Various studies have examined different material options for TCWS, and a brief summary is presented in Table 1. Although exhibiting remarkable potentials, major challenges are related to the need for expensive high quality heat and large temperature swing which can render the process less efficient.

An immediate extension of TCWS is reactive chemical-looping water splitting (RCLWS), in which, the reduction step

Table 1. Reported Total and Peak H_2 Production Rates for Two-Step Thermochemical Water Splitting[a]

| temp (°C; red/ox)	tot H_2 prodn (μmol/g)	peak H_2 rate (μmol/g/s)	feed H_2O (%)	oxygen carrier	ref
1500/800	278	6.8	44−52	CeO_2	6
1500/1500	126	1.0	15	CeO_2 (with Rh)	7
1350/1000	32	0.15	40	CeO_2	8
1500/1150	414	4.2	50, 84	CeO_2	9
1350/1000	28		81	CeO_2	10
1500/750	161		83	CeO_2 (10% Pr)	11
1400/1050	338		5.8	CeO_2 (25%Zr 1%Gd)	12
1300/800	109		30	$Ce_{0.15}Zr_{0.85}O_2$	13
1400/1050	467.7		38.3	CeO_2 (50% Zr)	14, 15
1500/500	210		84	$Ce_{0.9}Hf_{0.1}O_2$	16
1500/1000	153		83	CeO_2 (10% Mn)	17
1290/1000	62	16.4	21	CeO_2 (20% Zn)	18
1200/900	57		81	$Ni_{0.5}Mn_{0.5}Fe_2O_4$	10
1190/900	2120	9.4	56	Zn−Fe−O	19
1700/575	4270	9.1	56	FeO	20
1400/1000	195		5.8	$La_{0.5}Sr_{0.5}MnO_3$	21
1350/1000	307	1.3	40	$LaAlO_3$ (with Sr, Mn)	8
1400/1000	407	5.6		$La_{0.5}Ca_{0.5}MnO_3$	22

[a]Note some studies tested various material compositions for repeated cycles. The highest values are chosen and listed here for comparison. The conversion of the H_2 production unit from mL/g to μmol/g utilizes the ideal gas law at standard temperature and pressure (25 °C, 1 atm).

Table 2. Reported Total and Peak H_2 Production Rates for CLWS

temp (°C; red/ox)	tot H_2 prodn (μmol/g)	peak H_2 rate (μmol/g/s)	feed H_2O (%)	oxygen carrier	reducer	ref
800/800	3460	4.8	77	Fe_2O_3	CH_4	29
900/900	4140	8.1	30	Fe_2O_3	H_2	30
900/900	8900	34	31	Fe_2O_3 (with 5% CeO_2)	H_2+CO	31
800/800	47	0.36	5.5	Cu (with Co Pr)	H_2	32
650/350	150		20	CuO	H_2+CO	33
900/800	11300		20	$CuFe_2O_4$	CH_4	34
900/700	12000		31	$Cu_{0.7}Fe_{2.3}O_4/Ce−ZrO_2$	CH_4	35
900/800	2780		31	$CuFe_2O_4/ZrO_2$	CH_4	36
900/800	2130		31	$CuFe_2O_4/CeO_2$	CH_4	36
900/800	3000		47	$Ni_{0.39}Fe_{2.61}O_4$ (with ZrO_2)	CH_4	37
750/750	3500	3.8	20	WO_3 (with CeO_2, ZrO_2)	CH_4	38
800/500	840	0.29	2.4	$Ce_{0.8}Zr_{0.2}O_2$ (with Pt)	CH_4	39
850/700	500	1.1	83	CeO_2	CH_4	40
850/700	1580	1.3	83	$Ce_{0.7}Zr_{0.3}O_2$	CH_4	41
800/800	326	0.65	27	10 wt % CeO_2/ZrO_2	CH_4	42
800/700	1020	1.0	83	CeO_2 (30% Fe_2O_3)	CH_4	43
1000/1000	1240	160	26	CeO_2	H_2	this study
700/700	260	60	26	CeO_2	H_2	this study

is replaced by a fuel reduction reaction:

reduction step with fuel:

$$Me_xO_y + CH_4 \rightarrow Me_xO_{y-1} + CO + 2H_2 \qquad (3)$$
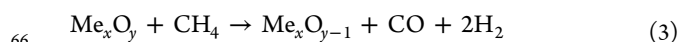
The utilization of fuel ensures an enhanced catalytic reaction at lower temperature with significantly improved extent of OC reduction and, hence, larger oxygen carrying capacity. The required high quality heat and large temperature swing could be replaced by an isothermal redox operation, hence leading to a much reduced cost, enhanced stability,[23−26] and improved system efficiency.[27,28] In contrast to TCWS, the net reaction, combining eqs 2 and 3, is a fuel reforming reaction, where a fuel is selectively oxidized to form hydrogen and syngas. In the case of natural gas, the syngas stream has a H_2:CO close to 2:1, ideal for the production of H_2 (after shift), methanol, or liquid fuel via Fischer−Tropsch process with CO_2 separation. With the abundance and low price of natural gas, RCLWS offers a simple and promising solution for co-producing hydrogen and syngas.

Several studies have examined various metal oxide candidates for RCLWS, including ceria, copper, ferrites, tungsten, and perovskites, etc. The reported H_2 production rates and total production using RCLWS are summarized in Table 2. It is generally observed that the use of ceria as an OC leads to higher H_2 production because of its fast surface kinetics, high oxygen ionic diffusivity, large oxygen carrying capacity, and robust structural stability. The ability of ceria to accommodate high surface active site concentrations facilitates a relatively quick surface ion-incorporation process.[44,45] The large nonstoichiometry capacity allows it to effectively adsorb and release oxygen as it responds to the operating conditions. This property has been exploited in a large number of applications,[46,47] including three-way catalyst, solid oxide fuel cells, and electrolyzers. For the same reason, CeO_2 has been suggested as a promising OC candidate for RCLWS.
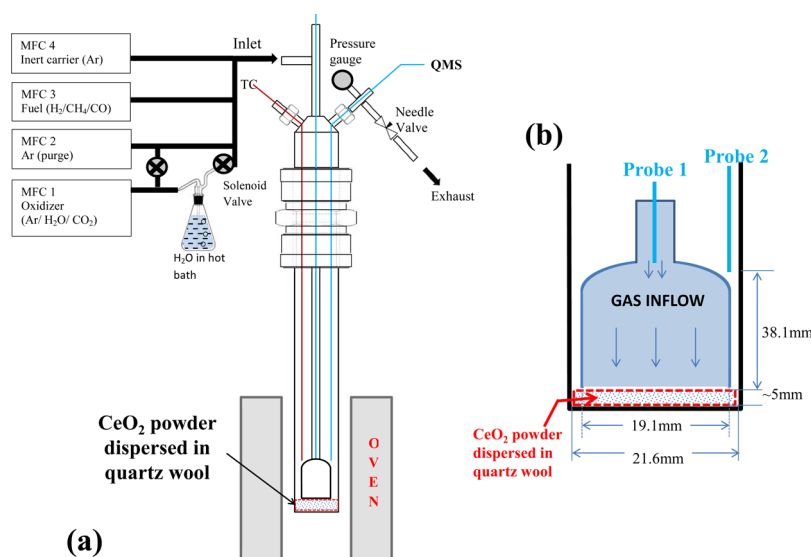
Figure 1. (a) Schematics of the experimental setup. (b) Schematics of the expansion tube, the sample, and the gas flow. Probe 2 is located close to the outer tube, about 1−2 mm above the top of the expansion section. Note that the y-direction of the drawing in panel b is compressed by 2.5 times as compared to x-axis for a better demonstration.

The bulk-phase properties of ceria-based materials have been widely studied. The physical, chemical, and electrochemical properties of pure and doped ceria at equilibrium have been examined and documented.[47−49] Recently, there is an increasing effort toward a better understanding of the surface-oriented defect chemistry of ceria, owing to the growing interests in fuel cells, electrolyzers, and water splitting.[45,50] Density functional studies examined surface defect formation and the energy landscape of the redox process.[51−53] In situ techniques, such as in situ X-ray photoelectron spectroscopy (XPS), have emerged recently and have been successfully applied to ceria.[44,45,54−56] The majority of the work concentrated on the surface and intermediate species at equilibrium. Despite the recent efforts in developing analytical models for reaction kinetics,[57−60] the fundamental surface redox pathway of ceria is not well understood. The complexities involved in the interactions of mobile ions, and electrons between the bulk and the surface, along with the adsorbates and electrostatic fields remain yet unresolved. Applying ceria in RCLWS requires a good knowledge of the time-resolved reactivity under conditions relevant for its application (temperature and gaseous composition), which is still missing.

In this work, we investigate the ceria redox mechanism with an emphasis on the surface ion-incorporation kinetics pathway, using a detailed time-resolved measurement under conditions relevant for RCLWS. Isothermal redox cycles of CeO_2 nanopowder are carried out in a button cell reactor in the temperature range 600−1000 °C. H_2 is used as a surrogate fuel in this study in order to explore the fundamentals of redox reactions on ceria. The reaction kinetics is determined by quantifying the flue stream composition using an online quadrupole mass spectrometer (QMS). H_2 is produced by water splitting during the oxidation cycle as a mixture of H_2O vapor and Ar is flown over CeO_2 samples. An order-of-magnitude higher hydrogen production rate is observed as compared to the state-of-the-art TCWS (Table 1) and RCLWS (Table 2) methods, resulting from the utilization of fine ceria nanopowder, which also ensures a surface-reaction-limited process. Kinetic models are subsequently developed to characterize the oxygen-ion-incorporation dynamics during the redox process. The model consists of a series of intermediate steps: adsorption/dissociation of gaseous reactant, charge transfer on the surface, and the bulk-to-surface transport. The model reveals the importance of the surface defect and its connection to the bulk phase. Driven by the difference of the defect formation energy, the surface is enriched with the key defects (oxygen vacancy and polarons), consistent with the in situ observations reported in the literature.[44,45] With the proposed kinetics, the rate-limiting step is identified, and suggestions are obtained for the development of better materials in the future.

2. EXPERIMENT

The experimental setup consists of a gas delivery system, a control unit, a central quartz reactor tube, and a real time flue gas analysis system with an online mass spectrometer. The system layout and the details of the reactor are shown in Figure 1.[61] Four Brooks GF40 MultiFlo digital thermal mass flow controllers (MFCs) are used for the gas flow control. The reactor is made of a quartz tube positioned inside an ATS 3210 split tube furnace that provides an isothermal environment up to 1100 °C. As shown in Figure 1b, the reactor consists of an outer tube (305 mm length, 25.4 mm outer diameter (o.d.), and 21.6 mm inner diameter (i.d.)), and an inner concentric 6.4 mm o.d. quartz tube with an expanding section of 19.1 mm o.d., 38.1 mm length. Gases flow through the central tube, impinge on the bottom of the outer tube, and exit reversely through the exhaust. Capillary probes made of quartz (0.53 mm i.d., 0.80 mm o.d.) are used to sample minute amounts of gases, before and after reactions. The probe sampling the exhaust flow is located close to the outer tube, around 1−2 mm above the top of the expansion section of the inner tube. A quadrupole mass spectrometer (HPR20 from Hiden Analytical Inc.) is used to analyze the flue gas composition. The QMS has a response time of less than 300 ms and a wide bandwidth of species detection capability.

Ceria powder from Sigma-Aldrich (99.95% purity) is used for the reaction study. Table 3 lists the properties of the sample. The BET surface area is 15.4 m^2/g, and the average size of the particle is 50 nm. A 100 mg amount of ceria powder is embedded in quartz wool and placed at the bottom of the outer quartz tube.

Table 3. Some Physical Properties of the CeO$_2$

property	value (unit)
density, ρ	7.22 g cm^{-3}
molar density, $\tilde{\rho}_{Ce}$	4.19×10^4 mol m^{-3}
lattice constant, a	0.54112 nm
surface molar density, $\tilde{\rho}_{Ce,s} = \tilde{\rho}_{Ce}a$	2.27×10^{-5} mol m^{-2}
melting point	2750 K
relative dielectric constant (0.5−50 MHz)	11
fresh sample	
bulk density	0.53 g cm^{-3}
purity	99.95%
specific surface area, s_0	15.4 m^2 g^{-1}
particle size	~50 nm
cycled sample	
specific surface area, s_1	3.99 m^2 g^{-1}
particle size	~200 nm

A lesser amount of sample is also tested (50 and 25 mg), and negligible difference is found in the obtained redox kinetics. The sample undergoes redox cycles, with argon as purging gas flowing in between. Oxidation is performed using a gas mixture of water vapor and argon. Ar is slowly bubbled through a 1 gallon bottle filled with deionized water maintained at 80 ± 0.5 °C in an insulated heat bath to prepare the oxidizing mixture. The steam mixture is further diluted with Ar to achieve the desirable H$_2$O concentration. The total flow rate into the reactor during the oxidation step is maintained constant at 337 cm^3(STP)/min, and the H$_2$O mole fraction is varied between 5% and 26%. H$_2$−Ar mixture is used for the reduction, with the total flow fixed at 350 cm^3(STP)/min and the H$_2$ mole fraction from 5% to 20%. While the ultimate technology objective is to use methane for reduction, H$_2$ is used as a surrogate to examine the process while simplifying the modeling of the redox reactions. All connecting stainless steel tubes are heated above 140 °C to avoid water condensation. The oxidation and reduction times are fixed at 2 min each for the base case. Before measurements, the samples are pretreated for 100 redox cycles at 1000 °C to reach periodic stationary states. Afterward, the measurements are taken from 1000 °C until 600 °C with a step of 50 °C. Each operating condition is repeated for at least five times, and results are averaged to reduce the noise. The measurements at 500 °C are also taken as a reference, although the reactivity is too low and can hardly be distinguished from background noise. Experiments with different oxidation and reduction conditions are also carried out to evaluate the effects on the H$_2$ production reactivity.

The redox process can be written as a reversible reaction:
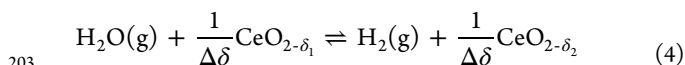
$$H_2O(g) + \frac{1}{\Delta\delta}CeO_{2-\delta_1} \rightleftharpoons H_2(g) + \frac{1}{\Delta\delta}CeO_{2-\delta_2} \qquad (4)$$

where $\Delta\delta = \delta_1 - \delta_2$ is the bulk-phase nonstoichiometry change. In order to derive the H$_2$ production rate based on the flue stream composition, we consider a control volume as outlined in Figure 1b. In the redox process, the production (or consumption) of 1 mol of H$_2$O leads to the consumption (or production) of 1 mol of H$_2$. Therefore, the total molar flow rate throughout the control volume remains constant; i.e., $\dot{n}_{in} = \dot{n}_{out}$. Thus, we can express the reaction rates as

oxidation:

$$\omega_{H_2} = \frac{X_{H_2,out}\dot{n}_{ox,out}}{m_{CeO_2}} = \frac{X_{H_2,out}}{m_{CeO_2}}\frac{P^0\dot{V}^0_{ox,in}}{RT^0} \qquad (5)$$

reduction:

$$\omega_{H_2O} = \frac{X_{H_2O,out}\dot{n}_{red,out}}{m_{CeO_2}} = \frac{X_{H_2O,out}}{m_{CeO_2}}\frac{P^0\dot{V}^0_{red,in}}{RT^0} \qquad (6)$$

$X_{H_2,out}$ and $X_{H_2O,out}$ are the measured mole fractions of the produced H$_2$ and H$_2$O at the exit. $\dot{n}_{ox,in}$ and $\dot{n}_{red,in}$ are the total molar inflow rates of the gas mixture for the oxidation and reduction, respectively. P^0, T^0, and V^0 are the pressure, temperature, and the total volumetric inflow rate at standard temperature and pressure (STP). The reaction rates (unit, μmol g^{-1}s^{-1}) are normalized by the total ceria sample m_{CeO_2}, i.e., 100 mg, used in the measurement. The derivation assumes a quasi-steady state and neglects the accumulation or depletion effect in the control volume. This is valid as the flow residence time is much shorter (~0.1 s) than the characteristic time of the redox conversion.[61] $\Delta\delta$ is calculated as

$$|\Delta\delta(t)| = n_O(t)/n_{CeO_2} \qquad (7)$$

where $n_O(t) = \int_0^t \dot{\omega}_{H_2} dt$ is the accumulated intake of oxygen ions. $n_{CeO_2} = m_{CeO_2}/M_{CeO_2}$ is the moles of ceria used in the experiment. M_{CeO_2} is the molecular weight.

3. THEORY

To model the reaction kinetics, ceria particles at cyclic stationary state are treated as identical spheres with diameter r_p = 100 nm (Table 3). The particle size is assumed to remain unchanged during the redox cycle, as CeO$_2$ is known to maintain its fluorite structure even under large nonstoichiometry at elevated temperatures.[47]

The overall reaction between the bulk ceria and the external gas-phase reactants may be written as[47−49]

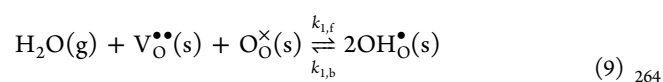$$H_2O(g) + 2Ce'_{Ce} + V_O^{\bullet\bullet} \rightleftharpoons H_2(g) + O_O^\times + 2Ce^\times_{Ce} \qquad (8)$$
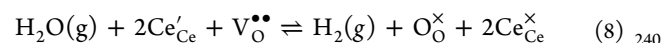
where $V_O^{\bullet\bullet}$ is a doubly charged oxygen vacancy, $O_O^\times$ is an oxygen ion on a normal site. Ce'_{Ce} denotes a polaron (a localized electron, Ce^{3+}), and $Ce^\times_{Ce}$ is a regular Ce^{4+} cation. Ce'_{Ce} and $V_O^{\bullet\bullet}$ are believed to be the major defects in the bulk as well as on the surface.[44,47−49]

Equation 8 merely describes the overall equilibrium between the defects in the bulk ceria and oxygen from the H$_2$O/H$_2$ environment. The electrochemical process, however, involves serial steps of important heterogeneous surface reactions, i.e., adsorption/dissociation of gaseous reactant forming adsorbates, ion/electron transfer on the surface, and association and desorption of products. The surface chemistry is further connected with the bulk phase via bulk-to-surface transport driven by the electrochemical potential gradient. Bulk-phase diffusion continues to adjust the spatial defect distribution and eventually equilibrates the sample with the environment. Figure 2 schematically highlights the key steps in the oxidation direction.

In the following two subsections, we will present the submodels for the surface chemistry and diffusion process, respectively.

Surface Chemistry. The surface water splitting and oxygen-incorporation reactions are modeled using a two-step mechanism (Figure 2a):[45,50−53]

R1:

$$H_2O(g) + V_O^{\bullet\bullet}(s) + O_O^\times(s) \underset{k_{1,b}}{\overset{k_{1,f}}{\rightleftharpoons}} 2OH_O^\bullet(s) \qquad (9)$$
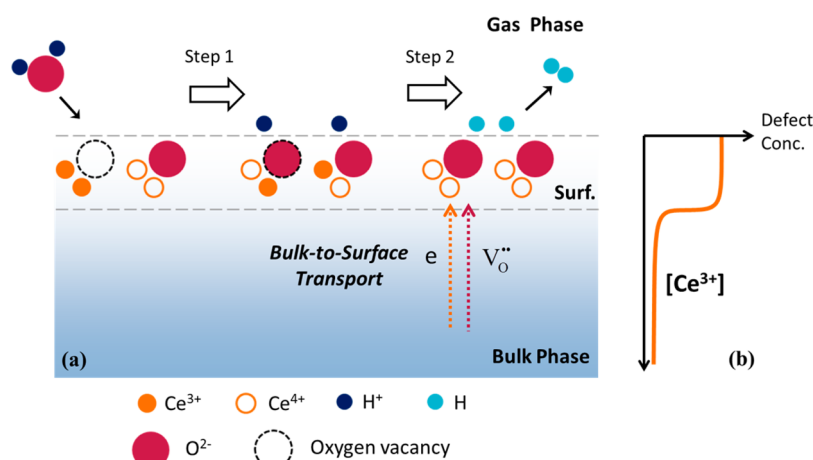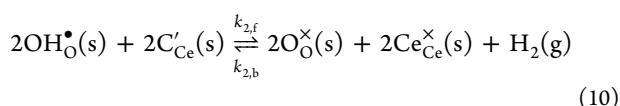
Figure 2. (a) Schematics of the water splitting pathway. The ion-incorporation surface process comprises the adsorption and dissociation of H_2O forming OH^- (R1) and charge transfer, association, and desorption of H_2 (R2). The heterogeneous chemistry is linked to bulk phase via the bulk-to-surface transport of the electron defect, e, and the oxygen vacancy defect, $V_O^{\bullet\bullet}$. (b) Schematics of the surface enrichment of Ce^{3+} relative to the bulk.

R2:

$$2OH_O^{\bullet}(s) + 2C'_{Ce}(s) \underset{k_{2,b}}{\overset{k_{2,f}}{\rightleftharpoons}} 2O_O^{\times}(s) + 2Ce_{Ce}^{\times}(s) + H_2(g) \tag{10}$$

$OH_O^{\bullet}$ is a hydroxyl ion group on an oxygen anion site. The surface reactions are assumed to occur only within the first unit cell layer on the surface, and s in the parentheses emphasizes this assumption. R1 describes the adsorption and dissociation process: a H_2O molecule is adsorbed onto an oxygen vacancy site and dissociates into a hydroxyl ion and an extra proton, which then bonds to an adjacent oxygen to form a second $OH_O^{\bullet}$ group. R2 describes the charge-transfer process, followed by the association and desorption of H_2.

Using the law of mass action, we express the species reaction rates for R1 and R2 as

$$r_1 = k_{1,f}p_{H_2O}[V_O^{\bullet\bullet}]_s[O_O^{\times}]_s - k_{1,b}[OH_O^{\bullet}]_s^2 \tag{11}$$

$$r_2 = k_{2,f}[OH_O^{\bullet}]_s^2[Ce'_{Ce}]_s^2 - k_{2,b}p_{H_2}[O_O^{\times}]_s^2[Ce_{Ce}^{\times}]_s^2 \tag{12}$$

In eqs 11 and 12, the brackets denote the mole of species per mole of CeO_2. The subscript, s, again, emphasizes that the concentrations of the reactant are taken on the surface. $k_{i,f}$ and $k_{i,b}$ denote the rate coefficients (unit, s^{-1}) of the aforementioned reactions and are assumed to follow the Arrhenius expression. Partial pressure of H_2 or H_2O in the gas phase is defined with respect to the reference value (i.e., 1 atm). Because of the high flow rates used in this study, the gas residence time through the control volume (Figure 1b) is much shorter (<300 ms) as compared to chemistry, and thus the reactant partial pressure on the surface is essentially identical to that in the gas phase as measured in the QMS. Therefore, the measured p_{H_2O} and p_{H_2} accurately represent the redox environment to which the ceria sample is exposed. At equilibrium, r_1 and r_2 are zero. This leads to the definition of the corresponding equilibrium constants K_1 and K_2.

A similar pathway has been discussed in the literature.[45,50−53] Feng et al.[45] emphasized the importance of the charge-transfer process, by further breaking R2 into $OH_O^{\bullet} + Ce'_{Ce} \rightarrow OH_O^{\times} + Ce_{Ce}^{\times}$, followed by the dissociation $2OH_O^{\times} = 2O_O^{\times} + H_2(g)$. Similar steps were calculated in a theoretical study by Marrocchelli and Yildiz.[51] Hansen and Wolverton[52] calculated the minimum energy pathway during R2 and concluded that the process may happen asymmetrically: Ce^{3+} hops close to $OH_O^{\bullet}$ and weakens the O−H bond; the weakly bonded proton then moves toward the adjacent $OH_O^{\bullet}$ and forms H_2 as the last Ce^{3+} is oxidized. Identifying the detailed elementary steps during R2 is beyond the scope of this study. Here we couple the charge transfer with the H_2 formation process and model it as a single step.

The governing equations for the surface species are written as

$$\frac{\partial \tilde{C}_i}{\partial t} = \dot{R}_i + \dot{J}_i \qquad i = OH_O^{\bullet}, V_O^{\bullet\bullet} \tag{13}$$

where $\tilde{C}_i$ is the species concentration on the surface, $\dot{R}_i$ is the production/consumption rate of species i, and $\dot{J}_i$ is the diffusion flux from the bulk phase. We proceed by coupling these species equations with the O- and Ce-site conservation equations and the electroneutrality condition:

O-site:

$$[V_O^{\bullet\bullet}]_s + [OH_O^{\bullet}]_s + [O_O^{\times}]_s = 2 \tag{14}$$

Ce-site:

$$[Ce'_{Ce}]_s + [Ce_{Ce}^{\times}]_s = 1 \tag{15}$$

electroneutrality:

$$2[V_O^{\bullet\bullet}]_s + [OH_O^{\bullet}]_s = [Ce'_{Ce}]_s \tag{16}$$

It is worth noting that the electroneutrality condition may break down in the space-charge region (SC) on the surface. The doubly charged oxygen vacancies along with the polarons form a double layer (i.e., positive charge from $V_O^{\bullet\bullet}$ on one layer and negative charge from Ce'_{Ce} on the other), creating a large disturbance of the spatial electrostatic potential gradient near the surface. This may lead to charge enrichment and simultaneous countercharge depletion in this region. However, Chueh and co-workers reported surface enrichment for both $V_O^{\bullet\bullet}$[45] and Ce'_{Ce}[44] in SC for Sm-doped CeO_2. Feng et al.[45] further quantified the contribution of the electrostatic potential gradient near the surface under redox conditions and concluded that the charge neutrality is preserved near the surface. As such, we adopt the electroneutrality assumption in this study for the

337 sake of simplicity. This assumption can be relaxed and examined
338 in depth in future study.

339   With eqs 14–16, the two species equations ($OH_O^\bullet$, $V_O^{\bullet\bullet}$)
340 describe the surface kinetics. Since the proton conductivity is
341 less pronounced compared to the major defects (vacancies
342 and polarons) in the bulk, we assume that all hydroxyl ions
343 are confined to the surface layer and hence neglect its diffusion.
344 Thus, we express the species conservation equations for the
345 surface hydroxyl group and the surface oxygen vacancy as

$$346 \quad \tilde{\rho}_{Ce,s} \frac{\partial [OH_O^\bullet]_s}{\partial t} = \tilde{\rho}_{Ce,s}(2r_1 - 2r_2) \tag{17}$$

$$347 \quad \tilde{\rho}_{Ce,s} \frac{d[V_O^{\bullet\bullet}]_s}{dt} = -\tilde{\rho}_{Ce,s} r_1 + \dot{j}_{V_O^{\bullet\bullet}} \tag{18}$$

348 Here $\tilde{\rho}_{Ce,s}$ is the surface molar density of the unit cell (unit,
349 mol m^{-2}). With the knowledge of $\dot{j}_{V_O^{\bullet\bullet}}$, eqs 17 and 18 complete
350 the description of the surface species evolution under the redox
351 conditions.

352   **Bulk-to-Surface Transport.** The conservation of a defect
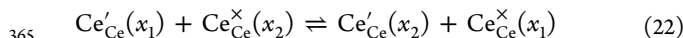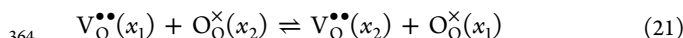353 species i can be expressed as

$$354 \quad \frac{\partial C_i}{\partial t} + \frac{1}{r^2} \frac{\partial}{\partial r}(r^2 \dot{j}_i) = 0 \qquad i = V_O^{\bullet\bullet}, Ce'_{Ce} \tag{19}$$

355 where C_i is the molar concentration and $\dot{J}_i$ the flux of the defect
356 species i. In eq 19, we assume a 1D spherically symmetric
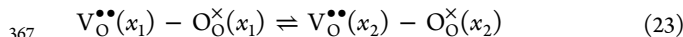357 diffusion. The flux density is expressed using the Nernst–Planck
358 equation:

$$359 \quad \dot{j}_i = -\frac{C_i D_i}{RT} \frac{\partial \tilde{\mu}_i^*}{\partial r} \tag{20}$$

360 where D_i is the diffusion coefficient, R the universal gas constant,
361 and T the temperature. $\tilde{\mu}_i^*$ is the electrochemical potential.
362   The diffusion process involves the exchange of defects between
363 two points, x_1 and x_2:[62]

$$364 \quad V_O^{\bullet\bullet}(x_1) + O_O^\times(x_2) \rightleftharpoons V_O^{\bullet\bullet}(x_2) + O_O^\times(x_1) \tag{21}$$

$$365 \quad Ce'_{Ce}(x_1) + Ce_{Ce}^\times(x_2) \rightleftharpoons Ce'_{Ce}(x_2) + Ce_{Ce}^\times(x_1) \tag{22}$$

366 By rearranging the above equations, we obtain equivalently

$$367 \quad V_O^{\bullet\bullet}(x_1) - O_O^\times(x_1) \rightleftharpoons V_O^{\bullet\bullet}(x_2) - O_O^\times(x_2) \tag{23}$$

$$368 \quad Ce'_{Ce}(x_1) - Ce_{Ce}^\times(x_1) \rightleftharpoons Ce'_{Ce}(x_2) - Ce_{Ce}^\times(x_2) \tag{24}$$

369 Equations 23 and 24 restate the diffusion process in terms of the
370 "defect elements", i.e., the structural defect minus the original
371 normal site.[62] Thus, $\tilde{\mu}_i^*$ for the oxygen vacancy and polaron can
372 be expressed as

$$373 \quad \tilde{\mu}_{V_O^{\bullet\bullet}}^* = \tilde{\mu}_{V_O^{\bullet\bullet}} - \tilde{\mu}_{O_O^\times} \tag{25}$$

$$374 \quad \tilde{\mu}_e^* = \tilde{\mu}_{Ce'_{Ce}} - \tilde{\mu}_{Ce_{Ce}^\times} \tag{26}$$

375 Here $\tilde{\mu}_i$ is the electrochemical potential for each species. We
376 note that the contribution of the normal sites ($\tilde{\mu}_{O_O^\times}$ and $\tilde{\mu}_{Ce_{Ce}^\times}$)
377 to the diffusion process cannot be neglected here, because the
378 redox conversion involves a large nonstoichiometry change, and
379 the availability of the normal sites significantly influences
380 diffusion.

381   We proceed by defining the electrochemical potential of the
382 structural defects and the normal sites as

$$383 \quad \tilde{\mu}_j = \mu_j^0 + RT \ln a_j + z_j F \phi \qquad j = V_O^{\bullet\bullet}, O_O^\times, Ce'_{Ce}, Ce_{Ce}^\times \tag{27}$$

384 where μ_j^0 is the chemical potential at the reference condition
385 and z_j the effective charge. ϕ is the internal electrostatic
386 potential. F is the Faraday constant. a_j is the activity, defined as

$$387 \quad a_j = \gamma_j \frac{C_j}{C_{ref}} \tag{28}$$

388 where γ_j is the activity coefficient and $C_{ref} =$ constant is a
389 reference molar concentration. Assuming that γ_j is independent
390 of concentration, we express the spatial derivatives of $\tilde{\mu}_j$ as

$$391 \quad \frac{\partial \tilde{\mu}_j}{\partial r} = \frac{\partial \mu_j^0}{\partial r} + RT \frac{\partial \ln C_j}{\partial r} + z_j F \frac{\partial \phi}{\partial r} \tag{29}$$

392 Substituting eqs 25–29 into eq 19 yields

$$393 \quad \frac{\partial [V_O^{\bullet\bullet}]}{\partial t} = \frac{1}{r^2} \frac{\partial}{\partial r} \left\{ \frac{r^2 [V_O^{\bullet\bullet}] D_{V_O^{\bullet\bullet}}}{RT} \left[\frac{\partial(\mu_{V_O^{\bullet\bullet}}^0 - \mu_{O_O^\times}^0)}{\partial r} \right. \right.$$
$$\left. \left. + RT \frac{\partial}{\partial r} \ln\left(\frac{[V_O^{\bullet\bullet}]}{[O_O^\times]} \right) + 2F \frac{\partial \phi}{\partial r} \right] \right\} \tag{30}$$

$$394 \quad \frac{\partial [Ce'_{Ce}]}{\partial t} = \frac{1}{r^2} \frac{\partial}{\partial r} \left\{ \frac{r^2 [Ce'_{Ce}] D_{Ce'_{Ce}}}{RT} \left[\frac{\partial(\mu_{Ce'_{Ce}}^0 - \mu_{Ce_{Ce}^\times}^0)}{\partial r} \right. \right.$$
$$\left. \left. + RT \frac{\partial}{\partial r} \ln\left(\frac{[Ce'_{Ce}]}{[Ce_{Ce}^\times]} \right) - F \frac{\partial \phi}{\partial r} \right] \right\} \tag{31}$$

395   Coupling with the Ce- and O-site conservation equations and
396 the electroneutrality condition:

397 O-site:

$$398 \quad [V_O^{\bullet\bullet}] + [O_O^\times] = 2 \tag{32}$$

399 Ce-site:

$$400 \quad [Ce'_{Ce}] + [Ce_{Ce}^\times] = 1 \tag{33}$$

401 elecroneutrality:

$$402 \quad 2[V_O^{\bullet\bullet}] = [Ce'_{Ce}] \tag{34}$$

403 Equations 30–34 formulate a complete description of the bulk
404 diffusion process.

405   The characteristics and the properties of the ceria sample
406 allow us to significant simplify these equations. The electronic
407 and ionic diffusivities ($D_{Ce'_{Ce}}$, $D_{V_O^{\bullet\bullet}}$) of ceria are very high
408 and bring the bulk defects to dynamic equilibrium during the
409 redox process. Using the diffusivity data reported in ref 63,
410 the characteristic time, t, for a diffusion-limited process from
411 the expression $t \sim R^2/4D$, is estimated to be less than 200 ms,
412 which is significantly faster compared to the surface chemistry.
413 A more rigorous calculation that takes into account the temporal
414 and spatial variation of the defect concentration is included in
415 Appendix A, which shows that the concentration variation caused
416 by the mass-transfer resistance is less than 4%. This estimation
417 indicates that the bulk diffusion within the ceria macroparticle
418 is fast enough that any spatial variations of $\tilde{\mu}_{V_O^{\bullet\bullet}}^*$ and $\tilde{\mu}_{Ce'_{Ce}}^*$ will be
419 readily removed via diffusion. As such, the conversion process is
420 essentially surface-reaction-limited. Thus, $\tilde{\mu}_{V_O^{\bullet\bullet}}^*$ and $\tilde{\mu}_{Ce'_{Ce}}^*$ remain
421 uniform throughout the particle while responding dynamically

to the changing environment. Equations 30 and 31 can be simplified as

$\tilde{\mu}^*_{V_O^{\bullet\bullet}}$ = constant:

$$\frac{\partial}{\partial r}(\mu^0_{V_O^{\bullet\bullet}} - \mu^0_{O_O^\times}) + RT\frac{\partial}{\partial r}\ln\left(\frac{[V_O^{\bullet\bullet}]}{[O_O^\times]}\right) + 2F\frac{\partial\phi}{\partial r} = 0 \tag{35}$$

$\tilde{\mu}^*_{Ce'_{Ce}}$ = constant:

$$\frac{\partial}{\partial r}(\mu^0_{Ce'_{Ce}} - \mu^0_{Ce^\times_{Ce}}) + RT\frac{\partial}{\partial r}\ln\left(\frac{[Ce'_{Ce}]}{[Ce^\times_{Ce}]}\right) - F\frac{\partial\phi}{\partial r} = 0 \tag{36}$$

However, the uniformity of the $\tilde{\mu}^*_{V_O^{\bullet\bullet}}$ and $\tilde{\mu}^*_{Ce'_{Ce}}$ does not necessarily means the same value of the defect concentration, $V_O^{\bullet\bullet}$ and Ce'_{Ce}, in the bulk and at the surface. In fact, owing to the difference of the standard chemical potentials ($\mu^0_{V_O^{\bullet\bullet}} - \mu^0_{O_O^\times}$ and $\mu^0_{Ce'_{Ce}} - \mu^0_{Ce^\times_{Ce}}$) between the bulk and the surface, a pronounced surface defect segregation phenomenon (see schematics in Figure 2b) has been observed in several studies.[44,45,55] Chueh et al.[44] reported a two-order-of-magnitude surface-to-bulk Ce'_{Ce} enrichment for Sm-doped ceria at 466 °C. Similar results were observed for the oxygen vacancies by Feng et al.[45] To model the surface effect, we assume that μ^0_j varies from the bulk ($r < r_p$) to the surface ($r = r_p$) according to a step function, as depicted in Figure 3. Thus, the defect concentration in the bulk phase is
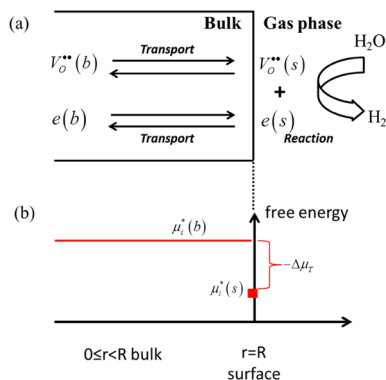

Figure 3. Schematics of (a) the bulk-to-surface transport model and (b) the difference of the defect formation energy. b and s in parentheses denote the defects in the bulk phase and on the surface, respectively.

uniform, and it connects dynamically to the kinetic process on the surface via diffusion. Eliminating ϕ in eqs 35 and 36 and integrating from the bulk to the surface yield

$$\frac{[V_O^{\bullet\bullet}]_s[Ce'_{Ce}]_s^2}{[O_O^\times]_s[Ce^\times_{Ce}]_s^2} \Bigg/ \frac{[V_O^{\bullet\bullet}]_b[Ce'_{Ce}]_b^2}{[O_O^\times]_b[Ce^\times_{Ce}]_b^2} = \exp\left(-\frac{\Delta\mu^0_T}{RT}\right) = K_T \tag{37}$$

where

$$\Delta\mu^0_T = (\mu^0_{V_O^{\bullet\bullet}} - \mu^0_{O_O^\times} + 2\mu^0_{Ce'_{Ce}} - 2\mu^0_{Ce^\times_{Ce}})_{surface}$$
$$- (\mu^0_{V_O^{\bullet\bullet}} - \mu^0_{O_O^\times} + 2\mu^0_{Ce'_{Ce}} - 2\mu^0_{Ce^\times_{Ce}})_{bulk} \tag{38}$$

Equation 37 essentially describes the transport equilibrium between the bulk and the surface, by combining reactions 23 and 24, as

$$V_O^{\bullet\bullet}(b) - O_O^\times(b) + 2Ce'_{Ce}(b) - 2Ce^\times_{Ce}(b)$$
$$\rightleftharpoons V_O^{\bullet\bullet}(s) - O_O^\times(s) + 2Ce'_{Ce}(s) - 2Ce^\times_{Ce}(s) \tag{39}$$

If we add $^1/_2O_2$ to both sides of eq 39, we arrive at the defect formation reaction:[47−49]

$$O_O^\times(b) + 2Ce^\times_{Ce}(b) \rightleftharpoons V_O^{\bullet\bullet}(b) + 2Ce'_{Ce}(b) + {^1/_2}O_2 \tag{40}$$

$$O_O^\times(s) + 2Ce^\times_{Ce}(s) \rightleftharpoons V_O^{\bullet\bullet}(s) + 2Ce'_{Ce}(s) + {^1/_2}O_2 \tag{41}$$

for the bulk and the surface, respectively. Therefore, $\Delta\mu^0_T$ is the difference in the formation energy of the defect between the surface (eq 41) and the bulk phase (eq 40), $\Delta\mu^0_T = \Delta\mu^0_{R,s} - \Delta\mu^0_{R,b}$, where $\Delta\mu^0_{R,b}$ and $\Delta\mu^0_{R,s}$ are the Gibbs free energy of reaction for eqs 40 and (41), respectively. $\Delta\mu^0_T$ can be further related to Δh^0_T, and Δs^0_T, as

$$\Delta\mu^0_T = \Delta h^0_T - T\Delta s^0_T \tag{42}$$

Creation of one defect involves breaking up four Ce−O bonds in the bulk, but fewer on the surface. Thus, defects are more energetically favored on the surface. On the other hand, the defect formation causes the relaxation of the adjacent atoms with reduced vibrational frequency and increased amplitude, leading to increased entropy.[62] The entropy increase is higher in the bulk, because more adjacent atoms are relaxed, and the relaxation from its dense-packed crystal is more dramatic. Thus, both Δh^0_T and Δs^0_T are negative. Based on the measurements by Chueh et al.,[44] we obtain $\Delta h^0_T = -113.7$ kJ mol^{-1}, and $\Delta s^0_T = -50.2$ J mol^{-1} K^{-1} for the Sm-doped ceria (see Appendix B for calculation).

Numerical Simulation. With the assumption of a uniform bulk defect concentration, and eq 37 to connect bulk to surface, we can simplify eq 18 by considering the conservation of the overall oxygen vacancy within the particle:

$$\frac{\partial}{\partial t}(\tilde{\rho}_{Ce}V_R[V_O^{\bullet\bullet}]_b) = -S_R\tilde{\rho}_{Ce,s}r_1 \tag{43}$$

where V_R, and S_R are the volume and the surface area of the particle, and $\tilde{\rho}_{Ce}$ is the molar density of the unit cell in the bulk. Equation 43 describes the fact that the surface splitting reaction leads to the consumption of oxygen vacancy. We note here that the moles of the oxygen vacancy on the surface is negligible compared to the bulk, and thus it is neglected from the left-hand side of eq 43.

Equations 17, 37, and 43 form the complete description of the redox process. The unknown (not all kinetic) parameters are $k_{i,f}$, K_i ($i = 1, 2$), Δh^0_T, and Δs^0_T. With the time-resolved profiles of $[H_2O]$ and $[H_2]$ measured using the QMS, the entire conversion process can be predicted. These equations are integrated numerically, and the predicted reactivity is compared to the experimental measurement. The unknown parameters are then varied to minimize the difference:

$$f = \sum_{all\,tests}\sqrt{\sum_{0\leq t\leq t^*}(\hat{\omega}_{predicted} - \hat{\omega}_{measured})^2} \tag{44}$$

Here the reaction rates ($\hat{\omega}_{predicted}$ or $\hat{\omega}_{measure}$) are normalized by the maximum rate in each test. The minimization is performed numerically in MATLAB using fminsearch solver.[64] The redox measurements at 600, 700, 800, 900, and 1000 °C are used to extract the unknown parameters. Δh^0_T and Δs^0_T for Sm-doped ceria calculated in Appendix B are taken as the initial guess, but

500 variations are allowed to account for the difference between
501 Sm-doped and undoped ceria. To ensure a global minimum,
502 the initial guess is randomly sampled over a wide range of
503 values (ln k_0 from −20 to 20, E from 0 to 200) for 200 tests,
504 and the results with minimum f are chosen.

4. RESULTS

CeO$_2$ Morphology Evolution and Cyclic Repeatability.
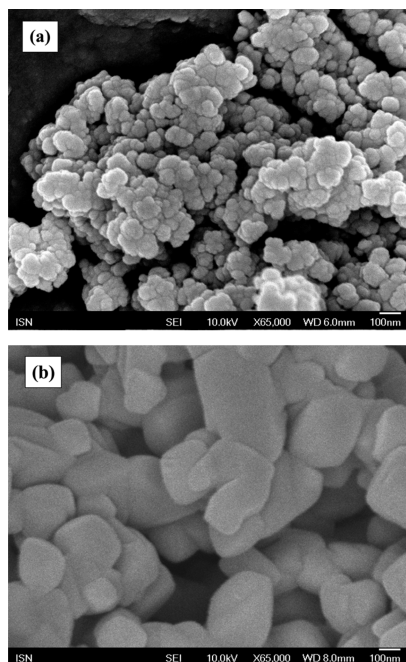506 Figure 4 shows the SEM images of the fresh (panel a) and aged

Figure 4. SEM images of ceria powder (a) before redox cycles and (b) after 100 redox cycles.

507 (panel b) ceria powder. It is found that the fresh sample
508 contains particles of size ∼ 50 nm, clumping together into
509 a mushroom-like structure. During pretreatment, the surface
510 area is reduced and the particles sinter into an interconnected

511 structure with a size ∼ 200 nm (based on the BET measure-
512 ment). This structural relaxation is caused by sintering during
513 the initial redox treatment (first 100 cycles). Samples after
514 additional 20 redox cycles are also examined, and the same
515 microstructure and redox rates are obtained, indicating that a
516 periodic and reversible stationary equilibrium is reached.
517   Figure 5 shows the profiles of H$_2$ and H$_2$O for three redox
518 cycles at 1000 °C. Reduction proceeds for 2 min with 14% H$_2$
519 at 350 cm^3(STP)/min, while oxidation with 26% H$_2$O for
520 2 min. Two min Ar purging is used in between to remove
521 residuals. H$_2$ spikes with the rise of H$_2$O, with the peak H$_2$ over
522 7%, roughly a quarter of the feed H$_2$O. After the peak, H$_2$ drops
523 quickly, and diminishes after 0.5 min. The H$_2$ near the end of
524 the oxidation phase is essentially zero. After oxidation, the ceria
525 sample is also tested with 1% O$_2$ (Ar balance), and no further
526 consumption of O$_2$ is observed. This indicates a complete
527 reoxidation of ceria with H$_2$O. Similarly, the produced H$_2$O
528 during reduction spikes at the beginning of each reduction
529 cycle. The peak H$_2$O reaches around 3%, approximately one-
530 fifth of the feed H$_2$ during reduction. H$_2$O decays slower as
531 compared to H$_2$ during oxidation, and approaches zero after
532 2 min, indicating a slower reactivity compared to oxidation.
533 The cycles are repeatable with no noticeable difference.
534 Figure 6 compares the total cumulative H$_2$ and H$_2$O production
535 during the oxidation and reduction steps, respectively, for eight
536 cycles measured at 1000 °C. The total H$_2$ production closely
537 matches with the H$_2$O production, indicating cyclic regener-
538 ability. The total produced H$_2$ is about 1250 μmol g^{-1} ceria,
539 corresponding to a $\Delta\delta$ of 0.215.
540   **Effect of Temperature.** Figure 7 compares ω_{H_2} and ω_{H_2O}
541 as a function of temperature from 500 to 1000 °C. In each plot,
542 the reaction rate exhibits a fast initial stage, followed by a
543 quick decrease. During oxidation, the fast initial rise of H$_2$
544 corresponds to the rapid ion-incorporation process with the
545 enriched surface oxygen vacancies, as shown in section 5. The
546 reactant concentration on the surface plays a significant role
547 in determining the maximum rate. For temperatures lower than
548 700 °C, H$_2$ production is limited, owing to the slow oxygen
549 removal kinetics and hence limited oxygen vacancy created
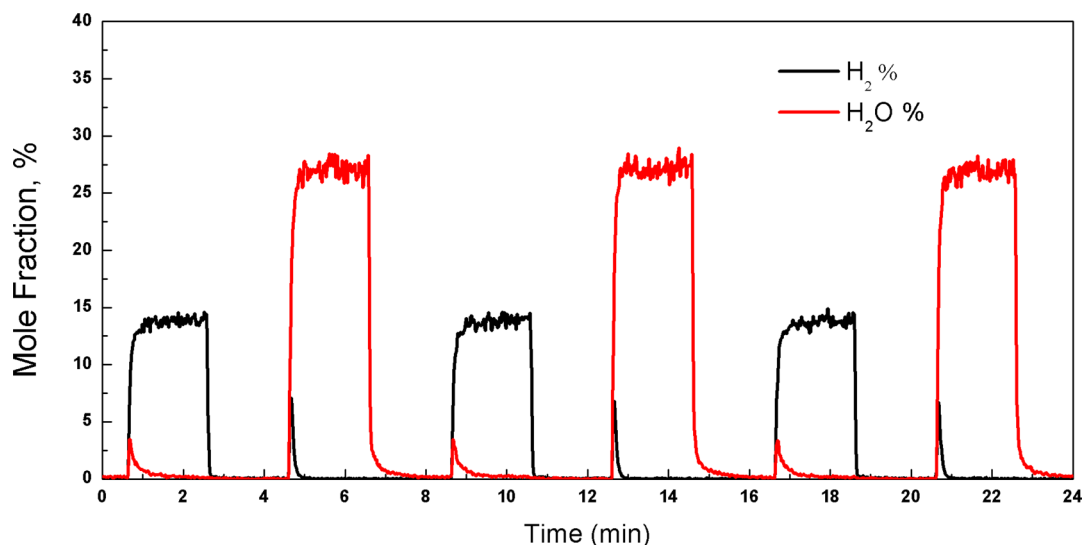550 in the previous reduction step. Increasing the temperature until

Figure 5. Three redox cycles at 1000 °C with 26% H$_2$O for oxidation and 13.7% H$_2$ for reduction. The redox step takes 2 min each, and the purging section takes 2 min in between. The total CeO$_2$ is 100 mg.
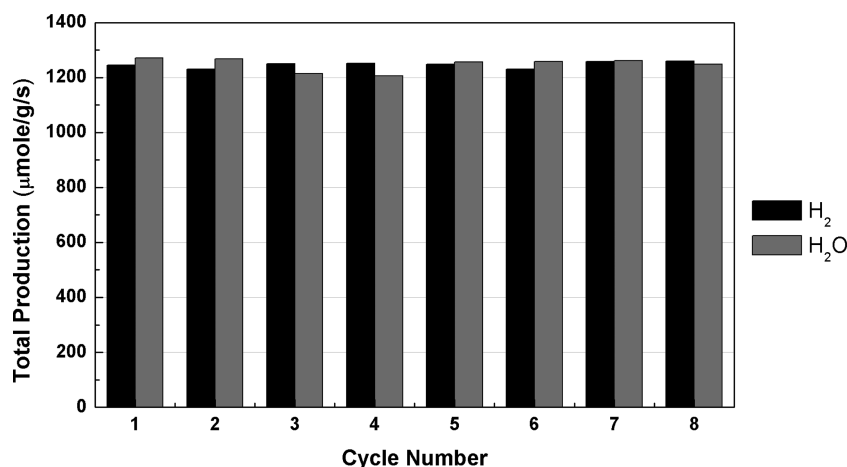
Figure 6. Total H_2 and H_2O production during the oxidation and reduction, respectively, for eight cycles at 1000 °C.
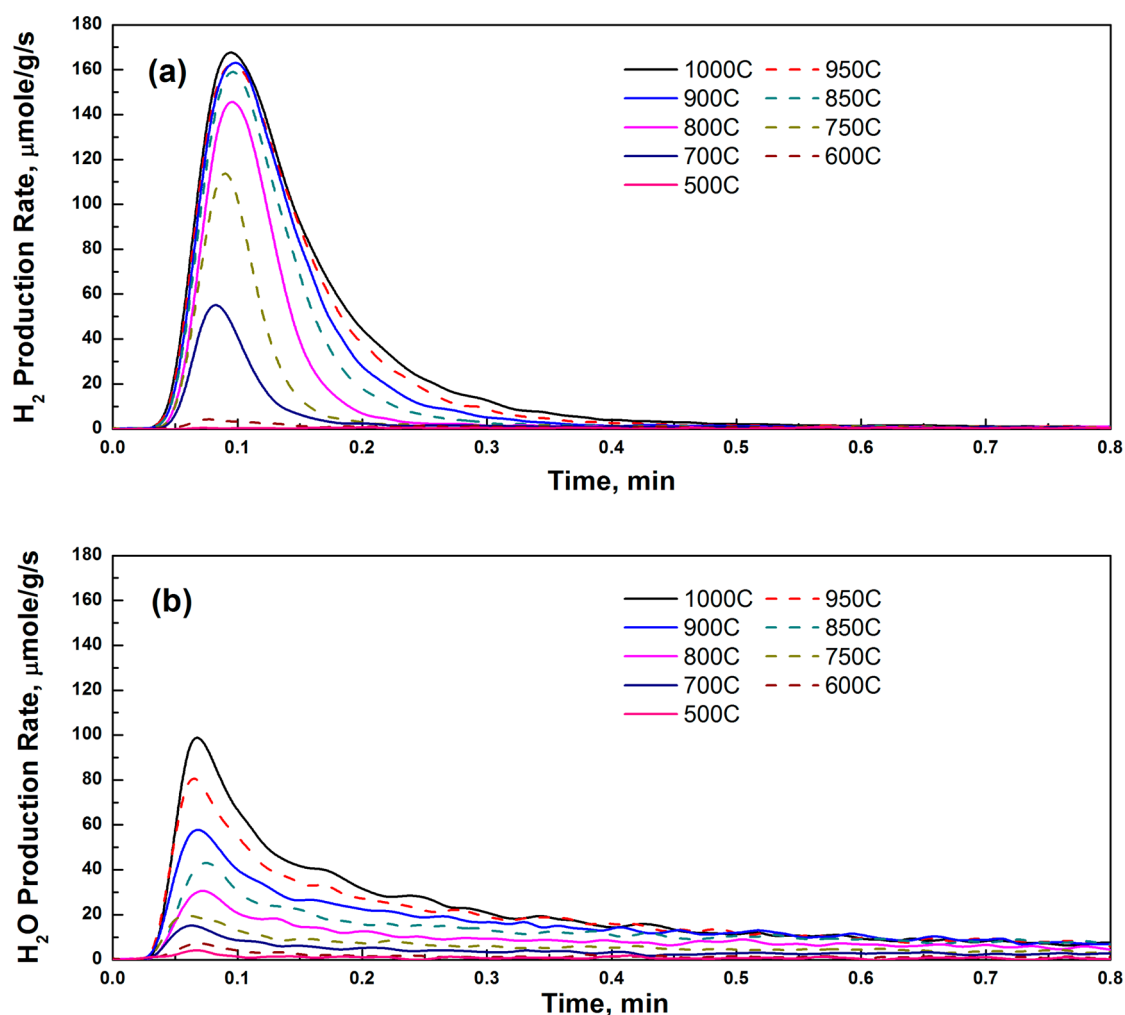

Figure 7. (a) H_2 production rate (μmol g^{-1} s^{-1}) during the oxidation step and (b) H_2O production rate (μmol g^{-1}s^{-1}) during the reduction step. Temperature is varied from 1000 to 500 °C. 26% H_2O at 337 cm^3(STP)/min is used for oxidation, and 14.3% H_2 at 350 cm^3(STP)/min is used for reduction. The uncertainties of the rate measurements are ±0.5 μmol g^{-1}s^{-1} for H_2 production, and ±0.75 μmol g^{-1}s^{-1} for H_2O production.

850 °C leads to a significant jump, and the peak rate doubles almost every 50 °C. Further increase in the temperature, however, only mildly improves H_2 production rates during the initial stage. As will be discussed in section 5, the nonlinear temperature dependence is caused by the surface defect segregation. Following the peak, H_2 production sharply decays and approaches zero after 0.5 min, exhibiting linear dependence on temperature, as it is mainly controlled by the available oxygen vacancy in the bulk phase.

Compared with oxidation, the reduction step is slower and more sensitive to temperature. A fast initial spike is again observed, followed by a slower decay. The peak occurs around
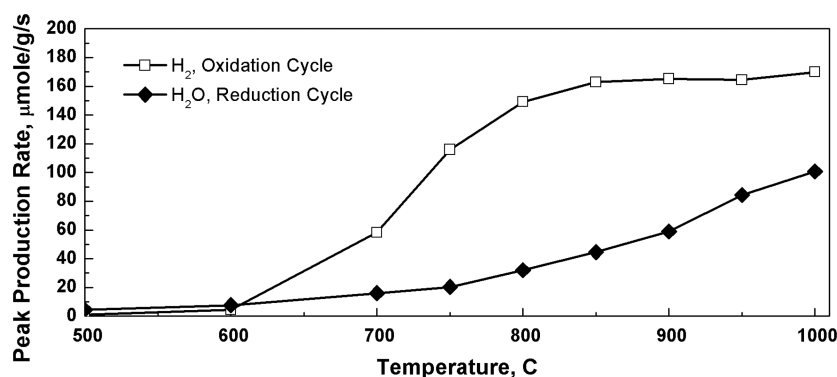
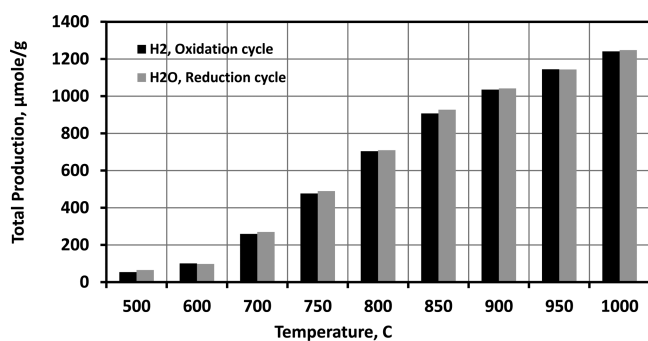**Figure 8.** Peak H_2 and H_2O production rates as a function of temperature during oxidation and reduction cycles.

Figure 9. Total H_2 and H_2O production as a function of temperature during oxidation and reduction steps.

563 0.08 min similar to that shown in Figure 7a, while the decay
564 continues even after 1 min (see Figure 5). During the initial

stage, the rise of ω_{H_2O} depends almost linearly on the tempera- 565
ture throughout the entire range, indicating a large activation 566
energy barrier. However, ω_{H_2O} profiles start to overlap during 567
the decay stage for temperature above 850 °C, as the removal 568
of oxygen essentially brings the surface closer to the beginning 569
of the oxidation phase, where the segregation effect reduces the 570
difference among different temperatures. 571

Figure 8 emphasizes the observed behavior of the peak rates at 572
varying temperature. The peak H_2 rate exhibits a sigmoidal profile 573
with a rapid increase around a threshold temperature of 700 °C, 574
while the peak H_2O rate continuously increases with temperature. 575
The total H_2/H_2O production during the 2 min oxidation/ 576
reduction process is illustrated in Figure 9. In all the cases, a close 577
match is found between the H_2 and H_2O production. Governed 578
by the temperature sensitive reduction step, the overall H_2 pro- 579
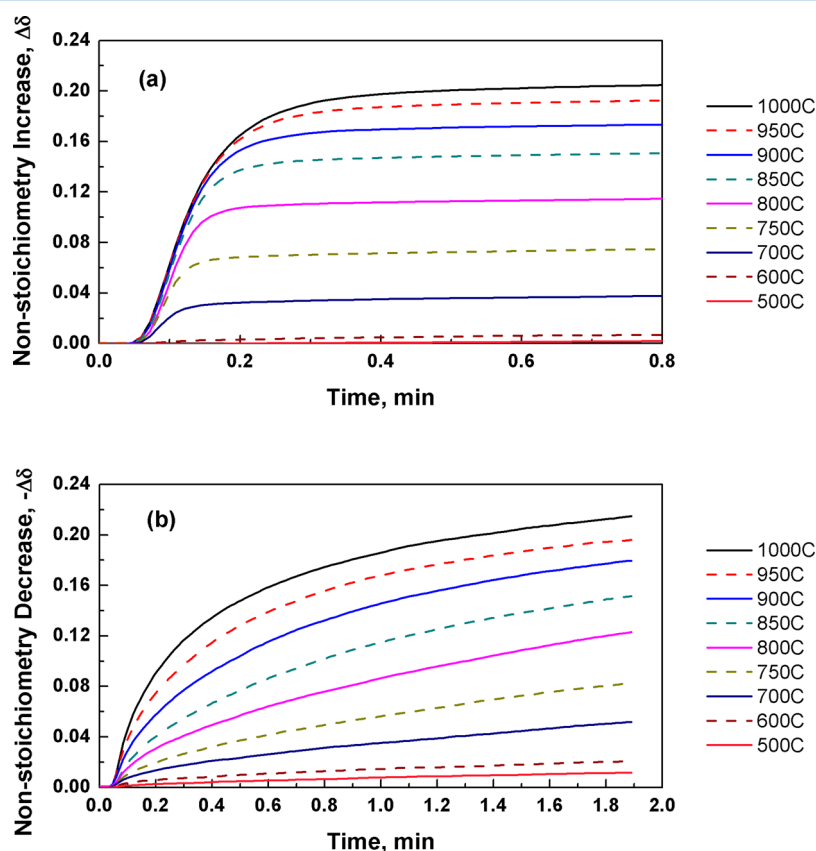duction rises continuously with temperature. Figure 10 compares 580

Figure 10. Nonstoichiometry change $\Delta\delta$ during (a) the oxidation step and (b) the reduction step as a function of temperature.
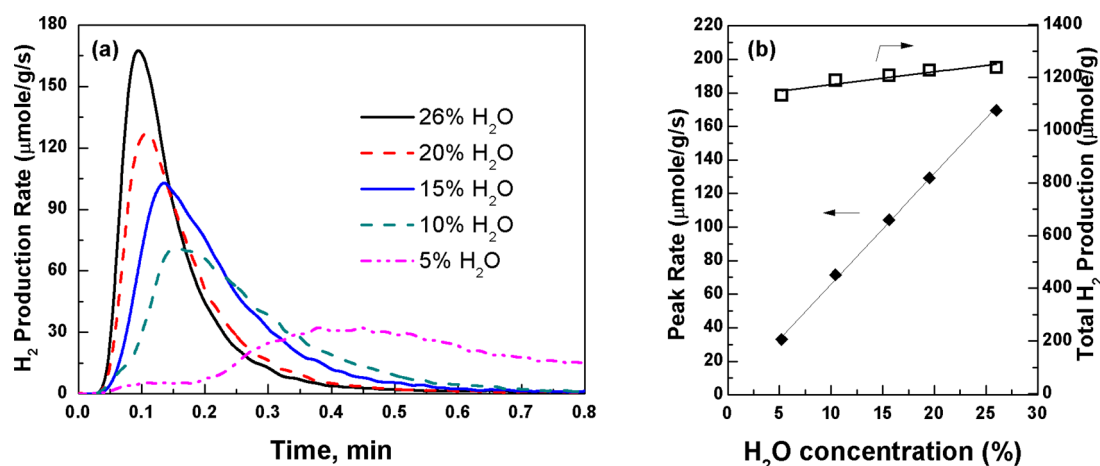
Figure 11. (a) Oxidation rate at different H_2O concentrations. (b) Peak rate and total production as a function of H_2O concentration. The temperature is fixed at 1000 °C. The H_2 concentration is fixed at 13.7% during reduction.
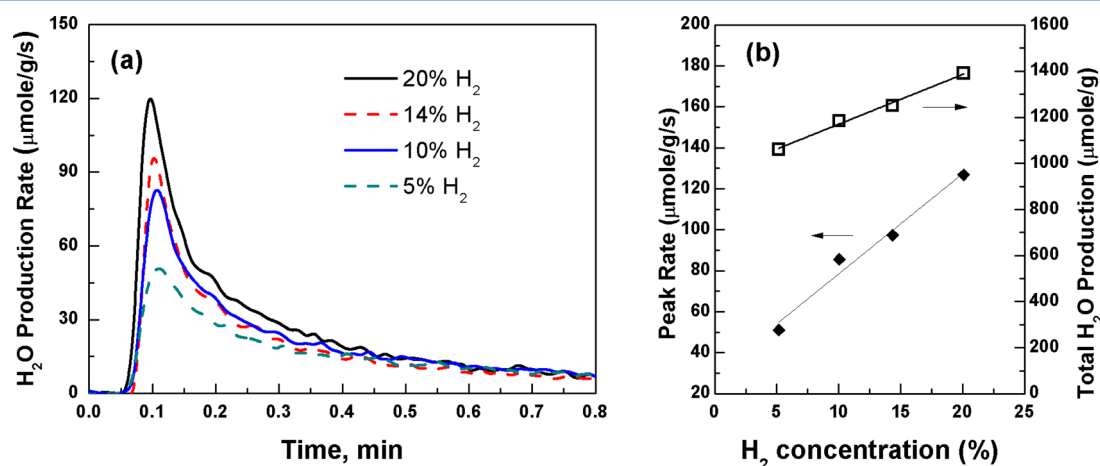

Figure 12. (a) Reduction rate at different H_2 concentrations. (b) Peak rate and total production as a function of H_2 concentration. The temperature is fixed at 1000 °C. The H_2O concentration is fixed at 26% during reduction.

Table 4. Fitted Kinetic Parameters for Both the Forward and Backward Reactions

	k (s^{-1})	
	reaction 1	reaction 2
forward	$1.3 \times 10^2 \exp((-7.0 \pm 7 \text{ kJ mol}^{-1})/RT)$	$1.5 \times 10^{14} \exp((-190 \pm 50 \text{ kJ mol}^{-1})/RT)$
backward	$8.2 \times 10^{14} \exp((-210 \pm 50 \text{ kJ mol}^{-1})/RT)$	$4.4 \times 10^4 \exp((-97 \pm 5 \text{ kJ mol}^{-1})/RT)$
equilibrium	$1.6 \times 10^{-13} \exp((203 \pm 50 \text{ kJ mol}^{-1})/RT)$	$3.4 \times 10^9 \exp((-93 \pm 50 \text{ kJ mol}^{-1})/RT)$

Table 5. Parameters for the Transport and Bulk Defect Equilibria

	CeO$_2$			Sm$_{0.2}$Ce$_{0.8}$O$_{1.9}$
	this work	ref 48[a]	ref 49	ref 44[b]
Δh_T^0 (kJ mol^{-1})	-107.6 ± 16.8			-95.7
Δs_T^0 (J mol^{-1} K^{-1})	-54.0 ± 11.9			-26.5
Δh_b^0 (kJ mol^{-1})	467.4 ± 8.9	455.2	450.2	373.2
Δs_b^0 (J mol^{-1} K^{-1})	172.9 ± 6.4	144.3	131.8	101.5

[a]Note that ref 48 reports varying enthalpy and entropy with δ; the values are averaged for $\delta = 0-0.05$. [b]The values are calculated based on the chemical potential of atom oxygen as reported in ref 44. See Appendix B for calculations.

the difference in the profiles of the nonstoichiometry $\Delta\delta$, as calculated in eq 7, during oxidation and reduction. The initial stage of oxidation ends within 15 s, but accounts for more than 80% of the overall change, and the residual oxidation only leads to a minor increase. Raising the temperature enlarges the overall oxygen carrying capacity, but the conversion follows a similar pattern. In comparison, reduction proceeds more gradually, and it is more temperature sensitive. The transition between the initial and residual stages is less obvious, and both stages equally contribute to the overall nonstoichiometry change. The reduction continues after 2 min although the rate is too slow to be of practical interest.

K

The measured peak H_2 rate is ~160 μmol g^{-1}s^{-1} at 1000 °C and 60 μmol g^{-1}s^{-1} at 700 °C (also included in Table 2 for comparison). The fast H_2 production rate is because of the fine particles, and hence large surface area, used in the measurements. Comparing to TCWS, the utilization of fuel in the reduction step creates many oxygen vacancies and hence leads to an enhanced H_2 production. The oxygen removal in reduction is the limiting step and is more temperature sensitive. 700 °C is the threshold temperature to achieve a large oxygen nonstoichiometry and hence enables a transition to a fast H_2 production rate in the following oxidation step. Therefore, 700 °C (or above) along with a longer residence time in reduction is beneficial.
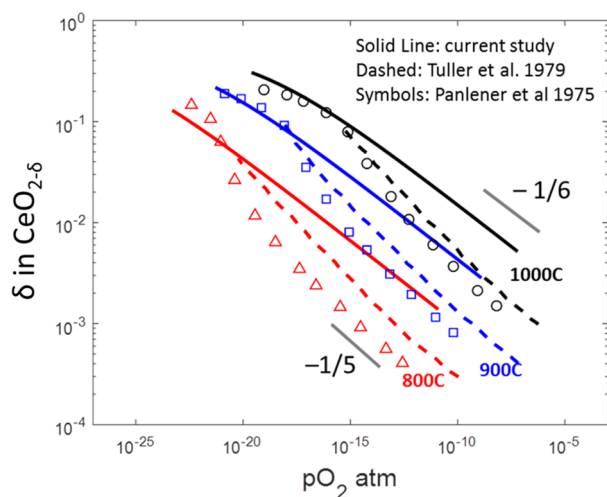
Effect of H_2O/H_2 Concentration. Figure 11 and Figure 12 show the effect of H_2O and H_2 concentration, respectively. The measured rates are plotted in panel a, while the peak rate and the total production are highlighted in panel b. ω_{H_2} becomes taller and narrower at higher H_2O concentration. The peak rate linearly depends on the H_2O concentration, while the total production remains the same. In contrast, a stronger reducing environment shifts the entire ω_{H_2O} curve outwardly and hence enlarges the overall oxygen carrying capacity. The peak rate also linearly depends on the H_2 concentration.

5. DISCUSSION

The kinetics and the defect equilibrium parameters derived in this study for undoped ceria are summarized in Table 4 and Table 5. The values of Δh_T^0 and Δs_T^0 are close to those obtained for Sm-doped ceria (see Appendix B). The bulk equilibrium for reaction 40 is also calculated by combining eqs 9, 10, and 39 along with the water splitting reaction, $H_2(g) + \frac{1}{2}O_2(g) = H_2O(g)$, as

$$K_b = \exp\left(-\frac{\Delta h_b^0 - T\Delta s_b^0}{RT}\right) = \frac{p_{O_2}^{1/2}[V_O^{\bullet\bullet}]_b[Ce'_{Ce}]_b^2}{[O_O^{\times}]_b[Ce_{Ce}^{\times}]_b^2}$$

$$= (K_1 K_2 K_T K_W)^{-1} \tag{45}$$

Here K_1, K_2, K_T, and K_W are the equilibrium constants for the surface reactions R1 and R2, the bulk-to-surface transport, and the water splitting reaction, respectively. The calculated bulk-phase equilibrium (Δh_b^0 and Δs_b^0) is in a close match with the literature,[48,49] as shown in Table 5. Figure 13 depicts isothermal bulk oxygen vacancy concentration as a function of the equivalent p_{O_2}, compared with the measurements reported by Panlener et al.[48] and Tuller and Nowick.[49] Quantitative agreement is found at large nonstoichiometry, although discrepancy

Figure 13. Isothermal oxygen nonstoichiometry as a function of p_{O_2} for CeO_2 from 800 to 1000 °C (solid lines). Dashed lines are based on the conductivity measurements by Tuller and Nowick.[49] Symbols are from Panlener et al.[48] Gray lines are for guiding the eyes.
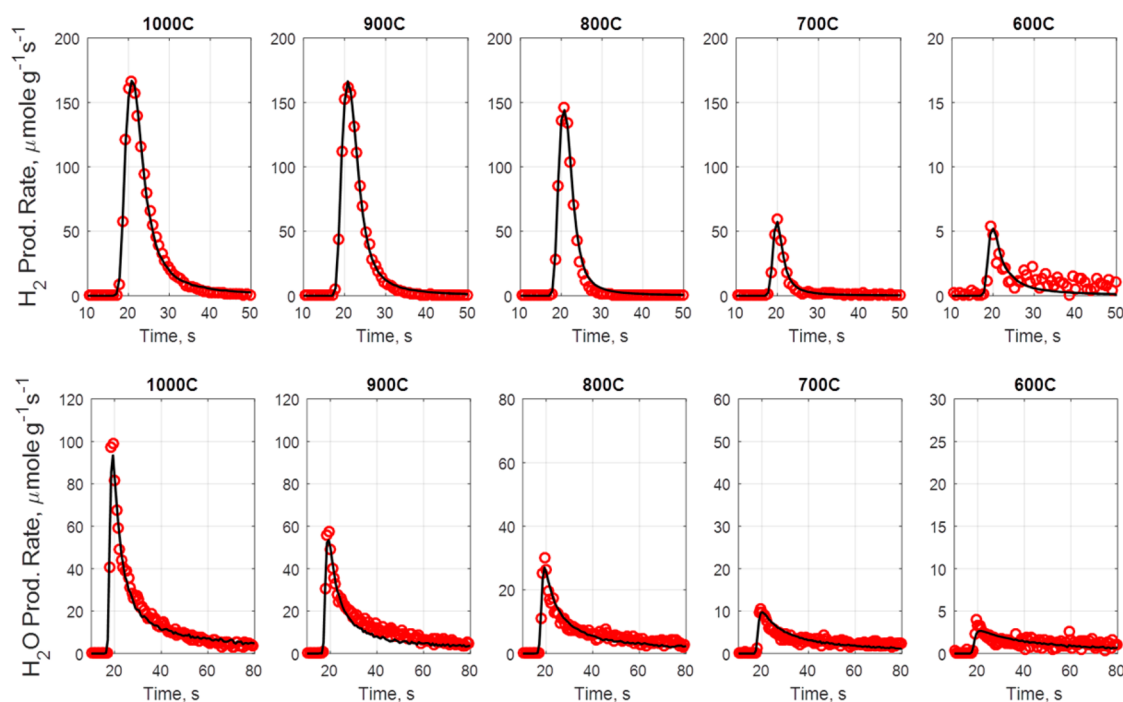
Figure 14. Comparison between the model predictions (lines) and the measurements (circles) for both oxidation (upper panels) and reduction (lower panels). The scales in the y-axis are different at lower temperature for clarity.

632 is seen when p_{O_2} is high, resulting from a slightly larger Δs_b^0.
633 Both ref 49 and the current study report a dependence of $-1/6$
634 near stoichiometry, while Panlener et al.[48] reported a depen-
635 dence close to $-1/5$, possibly due to the existence of impurities.[47]
636   Figure 14 shows a comparison between the measured reactiv-
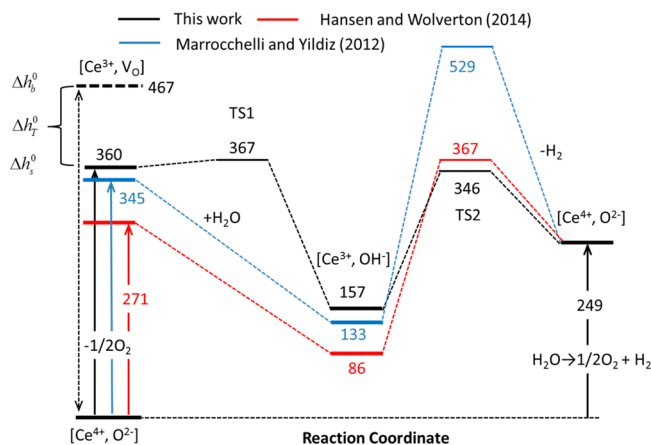637 ity and model predictions for both oxidation and reduction.

Figure 15. Energy landscape for the reaction pathway (black), and comparison with the theoretical calculations by Hansen and Wolverton[52] (red) and Marrocchelli and Yildiz[51] (blue).The dashed black line on the left side denotes the bulk-phase defect. Δh_b^0 and Δh_s^0 denote the defect formation energy for bulk (eq 40) and surface (eq 41), respectively, and Δh_T^0 denotes the difference. Unit is kJ mol^{-1}.

638 An excellent match is found for all cases. The predictions
639 well-characterize the spike−decay behaviors of both redox steps.
640 The temperature dependence is precisely represented; the subtle
641 difference between the reduction and oxidation steps is also
642 adequately captured.
643   Figure 15 shows the calculated energy landscape (black lines)
644 for the surface chemistry (see Table 4). The energy levels for
645 the intermediate species on the surface as well as the transi-
646 tion states are plotted in reference to the perfect crystal as the
647 ground state. R1 is highly exothermic with a minor barrier. The
648 second step is highly endothermic, and requires a significant
649 energy to break up the O−H bond. The intermediate species,
650 OH$_O^{\bullet}$, lies in a deep valley, and hence one may expect high
651 surface coverage at low temperature. The overall H$_2$ production
652 process (eq 8) is exothermic with the enthalpy of reaction
653 around -120 kJ mol^{-1}. The theoretical calculations by Hansen
654 and Wolverton[52] (red lines) and Marrocchelli and Yildiz[51]
655 (blue lines) are also included in this plot for comparison. Both
656 obtained similar reaction energy for the first step, although
657 they split it and simulated the adsorption and the dissociation
658 processes separately. Similarly, no substantial activation barriers
659 were found for R1 in either work. Marrochelli and Yildiz[51]
660 modeled the breaking of the O−H bond as a symmetric process
661 and reported a significant barrier around 400 kJ mol^{-1} for H$_2$
662 formation. In contrast, Hansen and Wolverton[52] identified an
663 asymmetric pathway with a much lower barrier (281 kJ mol^{-1}).
664 The current study reported a barrier around 200 kJ mol^{-1}.
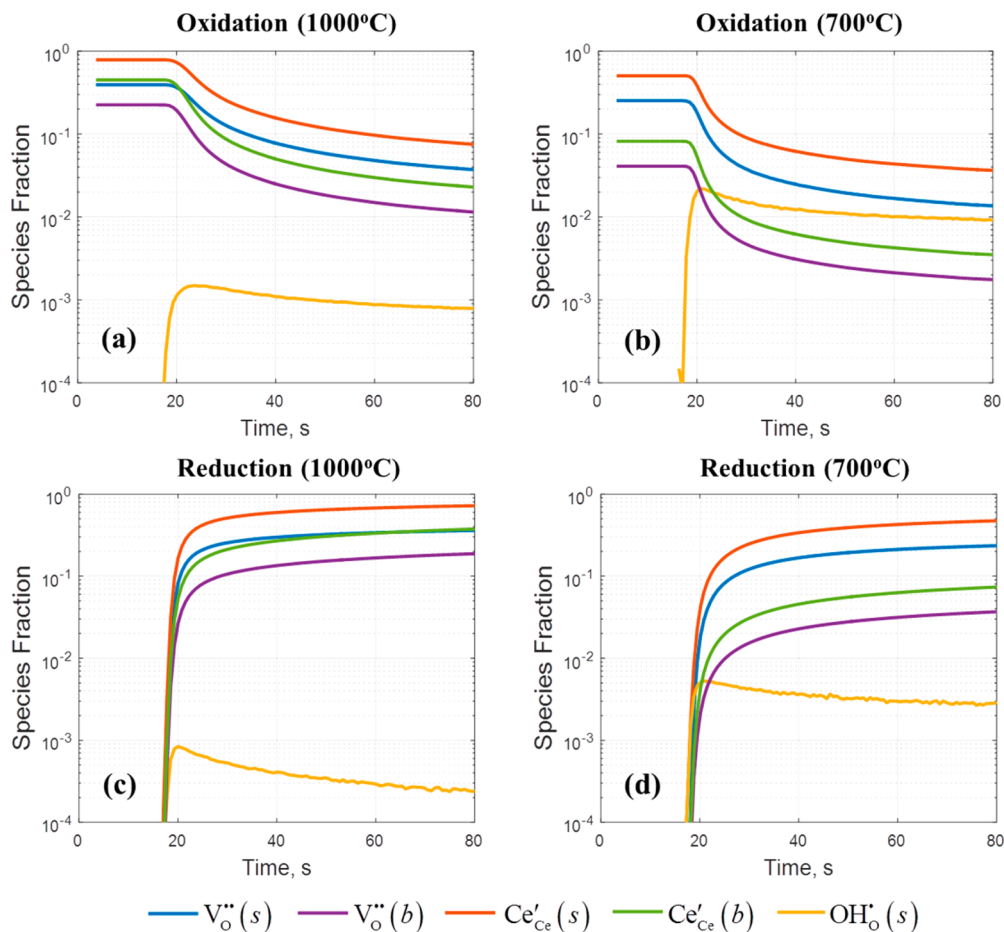665 The lower barrier may result from alternative fast desorption

Figure 16. Concentrations of the bulk and surface species for oxidation (a, b) and reduction (c, d) at 1000 and 700 °C.

pathways, especially at large nonstoichiometry when the surface defect vacancy concentrations are high. Marrocchelli and Yildiz[51] reported a similar overall energy of reaction (Δh_s^0 for eq 41) as in this study, while Hansen and Wolverton[52] reported a slightly lower value. The bulk-phase defect formation energy, Δh_b^0, is also included in Figure 15, and the difference between the bulk and the surface is Δh_T^0.

Figure 16 plots the species concentration in the bulk and on the surface. The reduction reaction starts from stoichiometry (complete oxidation from the previous step), while oxidation begins with the defects determined from the previous reduction step. During the oxidation step, all species undergo a quick decay, leading to a rapid H_2 production during the initial stage as observed in Figure 7. The initial stage is followed by a much slower decay as the conversion transits to the second stage where the species concentrations are mainly affected by the equilibrium with the H_2O/H_2 environment. Hydroxyl is quickly formed as the reaction starts and remains in a quasi-steady state during the rest of the process. Low temperature favors the formation of hydroxyl ions, owing to the large energy barriers as seen in Figure 15. The bulk defect concentrations are highly sensitive to temperature, as evident from the large Δh_b^0 shown in Table 5, leading to a significant difference between the high and the low temperature cases. On the other hand, the surface defect is less dependent on the temperature. In all cases, the concentrations on the surface are observed to be much higher than the bulk. The surface segregation effect is more significant at low temperature, causing over an order-of-magnitude improvement compared to the bulk phase. Similar behavior is observed during the reduction step, where the segregation effect is more pronounced near the end of conversion.

To further examine the surface segregation effect, Figure 17a shows the calculated equilibrium concentration of Ce'_{Ce} in the bulk and on the surface as a function of the effective p_{O_2}. Each line corresponds to the same range of $H_2O{:}H_2$ ratio, from 10^{-3} (reducing) to 10^3 (oxidizing). Under all conditions, the surface $[Ce'_{Ce}]$ value is significantly greater than the bulk, indicating that the surface is more reduced. The ratio between surface and bulk, as shown in Figure 17b, ranges from 1.5 to 15, favoring the low temperature. Apart from the difference in the absolute values, the temperature and oxygen dependence also differs remarkably between bulk and surface. $[Ce'_{Ce}]$ on the surface is only weakly sensitive to temperature and becomes almost the same above 800 °C (with $H_2O{:}H_2$), causing the overlap of the measured reaction rates during the first stage of oxidation (Figure 7a) and the second stage of reduction (Figure 7b). $[Ce'_{Ce}]$ in the bulk generally exhibits $-1/6$ dependence on the p_{O_2}, as expected from eq 45. On the other hand, the p_{O_2} dependence for surface $[Ce'_{Ce}]$ flattens from $-1/6$ with decreasing p_{O_2} and eventually goes to zero as the surface becomes fully reduced. This nonlinearity results from the reduced concentration of the normal sites ($O_O^\times$, $Ce_{Ce}^\times$ in eq 45) on the surface. As a result, the ratio in panel b exhibits a nonlinear pattern with p_{O_2}.

Figure 18 shows the forward and the backward reaction rates for the redox processes. At all temperatures, the H_2O adsorption and dissociation step (R1) during oxidation is much faster; equilibrium is quickly established and maintained throughout the rest of the conversion. In contrast, the ion/electron-transfer process (R2) is slower and its backward reaction rate is close to zero. This indicates that the reaction is limited by the charge-transfer process (R2), as also observed by Feng et al.[45]
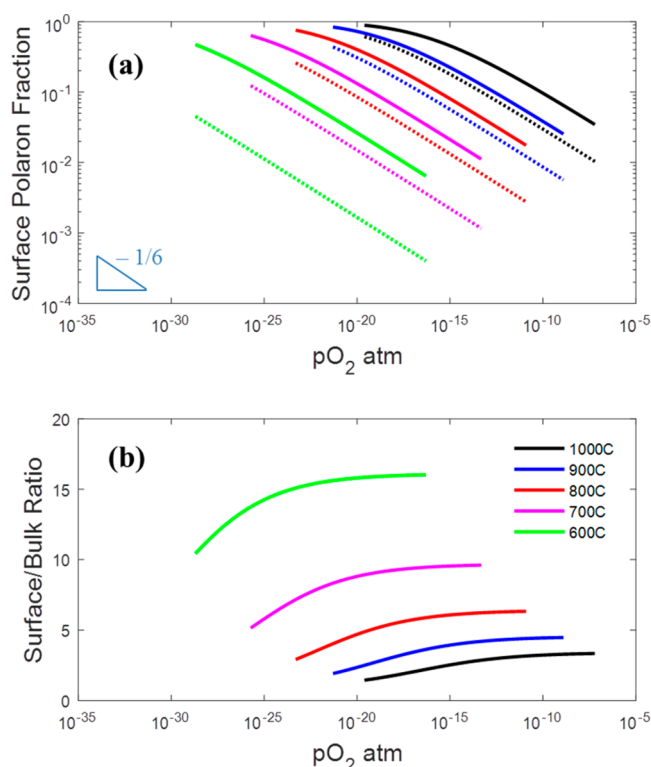

Figure 17. (a) Ce'_{Ce} concentration at equilibrium on the surface (solid) and in the bulk (dashed). Value of 1 corresponds to a complete reduction to the reduced 3+ state. (b) Ratio of the surface to bulk Ce'_{Ce} concentration.

Compared to oxidation, the reduction rate is much slower. The forward and backward rates for both steps are at similar magnitude, and equilibria are established during most of the conversion process. The low rates for R1 are mainly attributed to the low H_2O produced during reduction. A more reducing environment (e.g., higher H_2 concentration) effectively shifts the equilibrium backward, leading to more reduced ceria, as observed in Figure 12.

The surface segregation effect along with the plausible rate-limiting step observed in this study suggests directions for improving the water splitting activity of ceria and potentially other oxygen-incorporation materials. The reduction step is in general much slower, and it limits the redox capability at low temperature ($\leq$700 °C). Therefore, promoting the reduction step is essential to the low temperature water splitting process. On the other hand, the surface is nearly enriched with the defects at high temperature (>700 °C), and the overall H_2 production is constrained by the charge-transfer step. Thus, efforts should concentrate on accelerating the charge-transfer step at high temperature.

6. CONCLUSIONS

This work presents a detailed redox study with emphasis on identifying the surface ion-incorporation kinetics pathway. Time-resolved kinetics is measured for ceria nanopowder in a button cell reactor for 600−1000 °C at atmospheric pressure. The ceria sample is alternatively exposed to water vapor in the oxidation cycle to produce H_2 and H_2/Ar mixture in the reduction cycle to remove the lattice oxygen. The ceria sample undergoes structural and morphological changes during the initial redox treatment before reaching cyclic equilibrium.
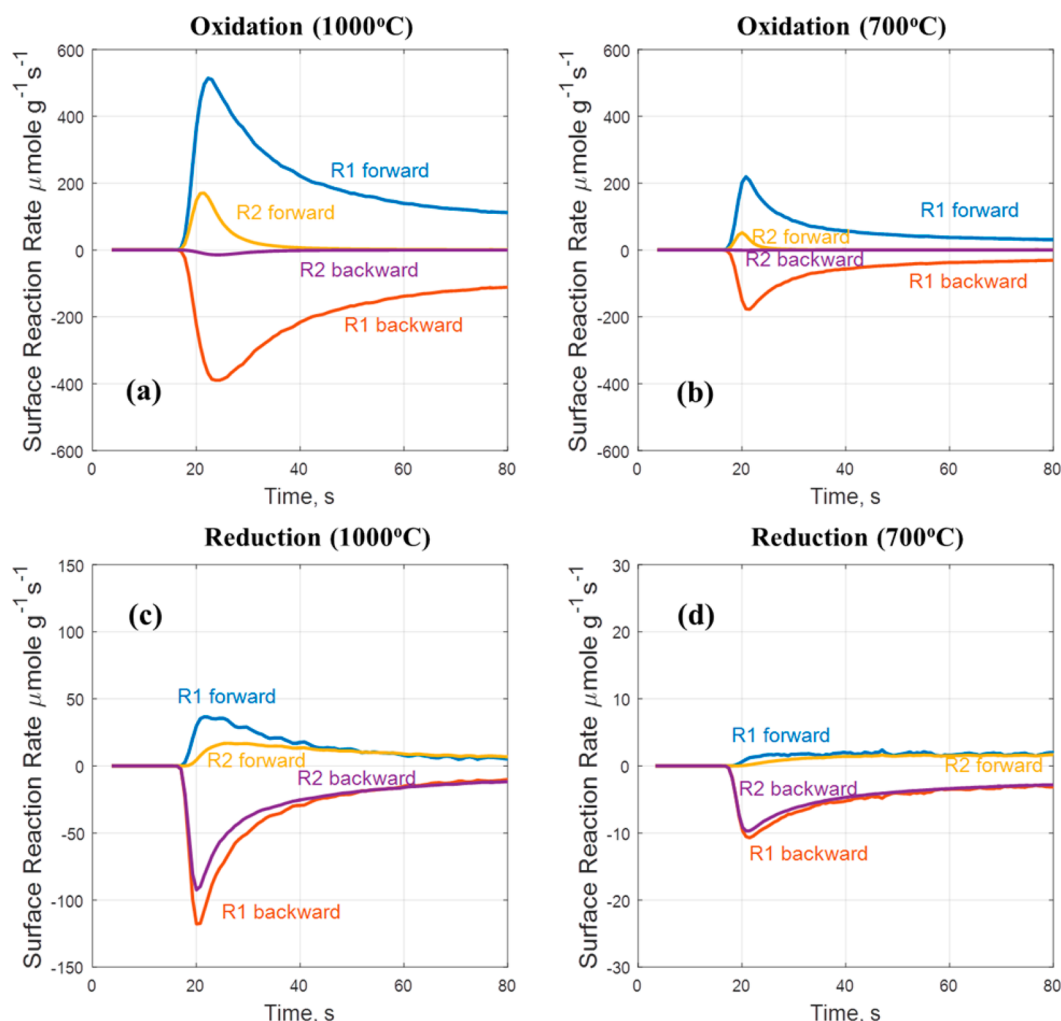
Figure 18. Surface reaction rates for both steps in oxidation (a, b) and reduction (c, d). The forward reaction rates are plotted as positive values, and the backward rates are negative. Note different scales are used in panels c and d for clarity.

We find an over 1 order-of-magnitude higher H_2 production rate compared to the state-of-art thermochemical water splitting and reactive chemical-looping water splitting studies. The high redox rates are attributed to the fine particles and hence large surface areas used in the study, which ensure a surface-limited-process. The peak rates measured are 160 μmol g^{-1}s^{-1} at 1000 °C and 60 μmol g^{-1}s^{-1} at 700 °C. The maximum nonstoichiometry change $(\Delta\delta)$ achieved is 0.215 at 1000 °C. It is found that the H_2 production rate depends weakly on temperature in the range 800−1000 °C, while the reduction process critically depends on the reaction temperature. Overall, reduction is the limiting step especially at low temperature, and it determines the total amount of the hydrogen produced in the following oxidation step.

The redox kinetics is modeled using a two-step surface chemistry while considering bulk-to-surface transport equilibrium. The proposed surface chemistry comprises an H_2O adsorption/ dissociation step and a charge-transfer step. Kinetics and equilibrium parameters are extracted and excellent agreement is achieved between the model predictions and the measurements. Driven by the difference in the free energy of formation, the surface defect concentration is found to be an order-of-magnitude higher than the bulk. The model reveals that the surface defects are abundant during the redox conditions, and the charge-transfer process is the rate-determining step for H_2 production.

The kinetic model along with the surface-controlled experiments provides a new approach to examine the redox pathways and defect equilibrium for alternative materials. The kinetics study also provides guidance for the design and the practical application of the chemical-looping water splitting technology: (1) finer particles are preferred to enable faster kinetics; (2) the operating temperature is recommended to be higher than the threshold 700 °C to ensure fast redox conversion; (3) an oxidation period less than 30 s suffices to regenerate the oxygen vacancy while a slightly longer residence time in reduction is beneficial.

■ APPENDIX A

The diffusion flux for $V_O^{\bullet\bullet}$ and Ce'_{Ce} can be expressed as

$$-\frac{J_{V_O^{\bullet\bullet}}}{\tilde{\rho}_{Ce}[V_O^{\bullet\bullet}]D_{V_O^{\bullet\bullet}}} = \frac{\partial[V_O^{\bullet\bullet}]}{\partial r}\left(\frac{1}{[V_O^{\bullet\bullet}]} + \frac{l}{2 - [V_O^{\bullet\bullet}]}\right) + \frac{2F}{RT}\frac{\partial\phi}{\partial r}$$

(A1)

$$-\frac{J_{Ce'_{Ce}}}{\tilde{\rho}_{Ce}[Ce'_{Ce}]D_{Ce'_{Ce}}} = \frac{\partial[Ce'_{Ce}]}{\partial r}\left(\frac{1}{[Ce'_{Ce}]} + \frac{l}{1 - [Ce'_{Ce}]}\right) - \frac{F}{RT}\frac{\partial\phi}{\partial r}$$

(A2)

Here we consider the region sufficiently away from the surface, such that the defect segregation effect is not important (i.e., μ_j^0 is constant).

Eliminating the electrostatic potential, we have

$$
\begin{aligned}
& -\frac{J_{V_O^{\bullet\bullet}}}{\tilde{\rho}_{Ce}[V_O^{\bullet\bullet}]D_{V_O^{\bullet\bullet}}} - \frac{2J_{Ce'_{Ce}}}{\tilde{\rho}_{Ce}[Ce'_{Ce}]D_{Ce'_{Ce}}} \\
& = \frac{\partial[V_O^{\bullet\bullet}]}{\partial r}\left(\frac{1}{[V_O^{\bullet\bullet}]} + \frac{1}{2 - [V_O^{\bullet\bullet}]}\right) \\
& \quad + \frac{2\partial[Ce'_{Ce}]}{\partial r}\left(\frac{1}{[Ce'_{Ce}]} + \frac{1}{1 - [Ce'_{Ce}]}\right)
\end{aligned}
\tag{A3}
$$

The electroneutrality assumption in the bulk phase requires that charge neutral:

$$
2[V_O^{\bullet\bullet}] = [Ce'_{Ce}]
\tag{A4}
$$

zero net current:

$$
2J_{V_O^{\bullet\bullet}} = J_{Ce'_{Ce}}
\tag{A5}
$$

With substitution of eqs A4 and A5 into A3, we have

$$
J_{V_O^{\bullet\bullet}} = -\tilde{D}\frac{\partial C_{V_O^{\bullet\bullet}}}{\partial r}
\tag{A6}
$$

where

$$
\tilde{D} = \frac{3D_{V_O^{\bullet\bullet}}D_{Ce'_{Ce}}}{D_{Ce'_{Ce}} + 2D_{V_O^{\bullet\bullet}}}\left(1 + \frac{[V_O^{\bullet\bullet}]}{6 - 3[V_O^{\bullet\bullet}]} + \frac{4[V_O^{\bullet\bullet}]}{3 - 6[V_O^{\bullet\bullet}]}\right)
$$

$\tilde{D}$ is the chemical (or ambipolar) diffusion coefficient, which critically depends on the operating condition, as well as the dopant/impurity concentrations. A range of values have been reported in the literature. To evaluate the contribution of the solid-phase diffusion to the overall redox process, we use the chemical diffusivity reported by Stan et al.,[63] which is in the lower range of the available data in the literature (see ref 57 for comparison) and, hence, leads to an estimation of the upper bound for the diffusional resistance.

The governing equations for $V_O^{\bullet\bullet}$ in the bulk phase can be expressed as

$$
\frac{\partial C_{V_O^{\bullet\bullet}}}{\partial t} + \frac{1}{r^2}\frac{\partial}{\partial r}(r^2 J_{V_O^{\bullet\bullet}}) = 0
\tag{A7}
$$

With substitution of eq A6 into eq A7, we have

$$
\frac{\partial C_{V_O^{\bullet\bullet}}}{\partial t} = \frac{1}{r^2}\frac{\partial}{\partial r}\left(r^2\tilde{D}\frac{\partial C_{V_O^{\bullet\bullet}}}{\partial r}\right)
\tag{A8}
$$

with initial condition

$$
C_{V_O^{\bullet\bullet}}(t = 0) = C_{V_O^{\bullet\bullet},0}
\tag{A9}
$$

and the following boundary conditions:

$$
s\tilde{D}\frac{\partial C_{V_O^{\bullet\bullet}}}{\partial r}\bigg|_{r=R} = \omega
\tag{A10}
$$

$$
\frac{\partial C_{V_O^{\bullet\bullet}}}{\partial r}\bigg|_{r=0} = 0
\tag{A11}
$$

In eq A9, s is the surface area, as listed in Table 3. ω is the surface H_2 (or H_2O) production rate (unit, mol s^{-1}). Equations A8–A11 are solved for the oxidation reaction of the particle with $R = 100$ nm. The peak H_2 production rate at each temperature is used to represent ω, and $\Delta\delta$ is used as the initial
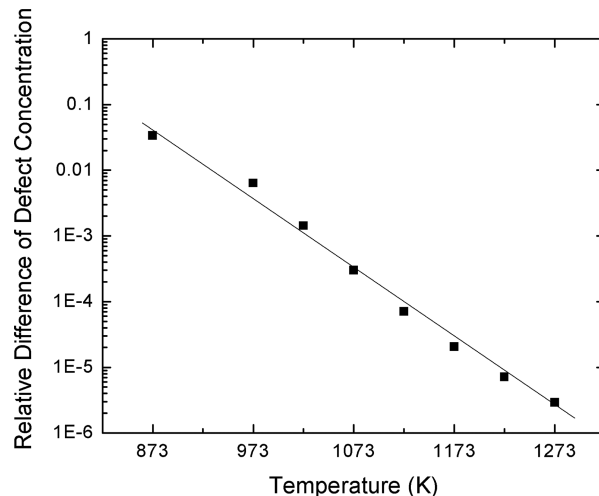

Figure 19. Relative difference of the oxygen vacancy concentration between the center and the surface. Line is for guiding the eyes.

condition. Calculation shows an upper bound for the diffusional contribution. Figure 19 plots the normalized difference of $C_{VO}^{\bullet\bullet}$ between the center and the surface:

$$
\Delta = \frac{C_{V_O^{\bullet\bullet}}(r = 0) - C_{V_O^{\bullet\bullet}}(r = R)}{C_{V_O^{\bullet\bullet}}(r = R)} \qquad \text{when } C_{V_O^{\bullet\bullet}}(r = R) = \frac{1}{2}C_{V_O^{\bullet\bullet},0}
\tag{A12}
$$

From Figure 19, the maximum difference is found to be less than 4% at 600 °C and reduces to less than 0.001% at 1000 °C. Calculation here indicates that the bulk diffusion is unlikely to be rate-limiting in the redox process.

■ APPENDIX B

Chueh et al.[44] measured both the bulk and the surface concentration Ce^{3+} (or Ce'_{Ce}) for $Sm_{0.2}Ce_{0.8}O_{1.9}$ under equilibrium for the temperatures at 466, 521, 586, and 650 °C. The authors compared the chemical potential of atomic oxygen for the surface and bulk and attributed the higher concentration of surface Ce^{3+} to the higher entropy of the surface oxygen. Here, we take into account the difference of the defect formation energy as well as the entropy and present a detailed analysis following an approach similar to that detailed in section 3 (see Figure 3),

The site conservation and electroneutrality conditions are

$$
[V_O^{\bullet\bullet}] + [O_O^{\times}] = 1.9
\tag{B1}
$$

$$
[Ce'_{Ce}] + [Ce_{Ce}^{\times}] + [Sm'_{Ce}] = 1
\tag{B2}
$$

$$
2[V_O^{\bullet\bullet}] = [Sm'_{Ce}] + [Ce'_{Ce}]
\tag{B3}
$$

In the bulk phase, $[Sm'_{Ce}]_b = 0.2$. By substituting eqs B1–B3 into eq 45, and fitting with respect to the measurements of the bulk $[Ce'_{Ce}]$ and $p_{o_2}^{1\backslash2}$, we obtain the equilibrium constant for the bulk-phase defects, K_b:

$$
K_b = \exp\left(-\frac{\left(379.5\frac{kJ}{mol}\right) - \left(97.1\frac{J}{mol\,K}\right)T}{RT}\right)
\tag{B4}
$$

The bulk-to-surface transport equilibrium is described by eq 37. The dopant concentration on the surface, $[Sm'_{Ce}]_s$, is in the range between 0.26 and 0.35, slightly greater than the bulk.

For simplicity, we use $[Sm'_{Ce}]_s = 0.3$. Note here the right-hand side of eq B1 becomes 1.85 for the surface ($Sm_{0.3}Ce_{0.7}O_{1.85}$).

By substituting eqs B1−B3 into eq 37, and comparing with the measurements of the surface $[Ce'_{Ce}]$ at given temperature and oxygen partial pressure, we obtain the equilibrium constant for the transport, $\Delta\mu_T^0$:

$$\Delta\mu_T^0 = \left(-113.7\,\frac{kJ}{mol}\right) - \left(-50.2\,\frac{J}{mol\,K}\right)T \tag{B5}$$

The model predictions are plotted in Figure 20 along with the measurements, and an excellent agreement is found for both the surface and the bulk defect concentrations.

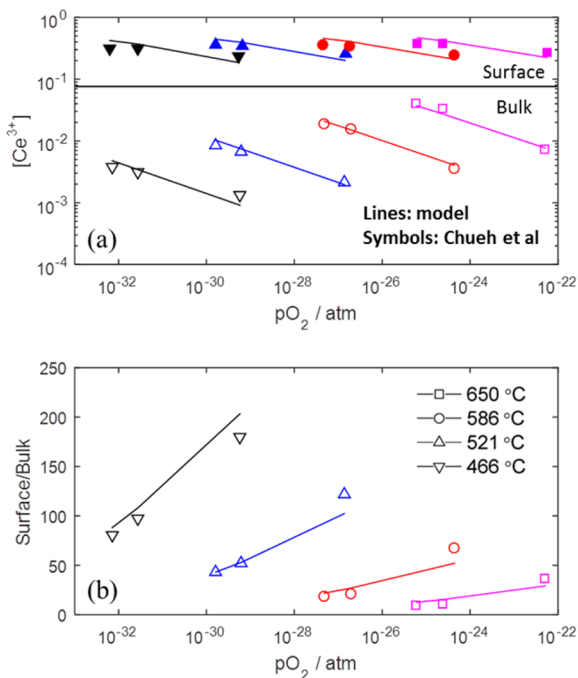**Figure 20.** (a) Comparison of the surface (closed) and bulk Ce^{3+} (open) concentrations between the measurements (symbols) by Chueh et al.[44] and the model predictions (lines). (b) Ratio of the surface to bulk Ce^{3+} concentrations. Symbols are from ref 44, and lines are from the modeling.

It is interesting to note that compared to the bulk, the surface has 30% less defect formation enthalpy and over 50% less defect formation entropy. The ratio of the surface-to-bulk Ce^{3+} is highest at low temperature and drops dramatically as the temperature is raised. Crossover, $\Delta\mu_T^0 = 0$, is reached when $T = 2265$ K, approaching the melting point.

Chueh et al.[44] reported the chemical potential of atomic oxygen for the surface and bulk, defined as

$$\mu_O = \frac{1}{2}\mu_{O_2} = \frac{1}{2}(\mu_{O_2}^0 + RT\ln p_{O_2}) \tag{B6}$$

where $\mu_{O_2}^0$ is the standard potential at 1 atm. μ_O can further be related to the partial molar enthalpy (H_O) and entropy (S_O) from $\mu_O = H_O - TS_O$. The reported H_O and S_O are -373.2 kJ mol^{-1} and -86.1 J mol^{-1} K^{-1} for $[Ce^{3+}]_{bulk} = 0.0071$, and -277.5 ± 28.7 kJ mol^{-1} and 28.7 ± 28.7 J mol^{-1} K^{-1} for $[Ce^{3+}]_{surf} = 0.36$.

To relate the partial molar free energy of the oxygen atom to the defect formation free energy, we consider the defect formation reaction, eqs 40 and 41, at equilibrium. The Gibbs free energy is

zero: $\Delta G = 0 = \mu_{V_O^{\bullet\bullet}} + 2\mu_{Ce'_{Ce}} + \frac{1}{2}\mu_{O_2} - \mu_{O_O^\times} - 2\mu_{Ce_{Ce}}$. With substitution of eqs 27 and B6, we obtain

$$
\begin{aligned}
\mu_O &= H_O - TS_O \\
&= -(\mu_{V_O^{\bullet\bullet}}^0 + RT\ln[V_O^{\bullet\bullet}] + 2\mu_{Ce'_{Ce}}^0 + 2RT\ln[Ce'_{Ce}] - \mu_{O_O^\times}^0 \\
&\quad - RT\ln[O_O^\times] - 2\mu_{Ce_{Ce}^\times}^0 - 2RT\ln[Ce_{Ce}^\times]) \\
&= -\left\{(h_{V_O^{\bullet\bullet}}^0 + 2h_{Ce'_{Ce}}^0 - h_{O_O^\times}^0 - 2h_{Ce_{Ce}^\times}^0)\right. \\
&\quad \left. - T(s_{V_O^{\bullet\bullet}}^0 + 2s_{Ce'_{Ce}}^0 - s_{O_O^\times}^0 - 2s_{Ce_{Ce}^\times}^0) + RT\ln\left(\frac{[V_O^{\bullet\bullet}][Ce'_{Ce}]^2}{[O_O^\times][Ce_{Ce}^\times]^2}\right)\right\}
\end{aligned}
\tag{B7}
$$

Therefore,

$$H_O = -\left(\Delta h^0 - \frac{1}{2}h_{O_2}^0\right) \tag{B8}$$

$$S_O = -\left(\Delta s^0 - R\ln\left(\frac{[V_O^{\bullet\bullet}][Ce'_{Ce}]^2}{[O_O^\times][Ce_{Ce}^\times]^2}\right) - 0.5s_{O_2}^0\right) \tag{B9}$$

where Δh^0 and Δs^0 are the defect formation energy and entropy. Based on the reported values for H_O and S_O, we obtain $\Delta h_b^0 = 373.2$ kJ mol^{-1} and $\Delta s_b^0 = 101.5$ J mol^{-1} K^{-1} for $[Ce^{3+}]_{bulk} = 0.0071$, and $\Delta h_s^0 = 277.5 \pm 28.7$ kJ mol^{-1} and $\Delta s_b^0 = 75.0 \pm 28.7$ J mol^{-1} K^{-1} for $[Ce^{3+}]_{surf} = 0.36$. Therefore, the differences between the surface and the bulk are $\Delta h_T^0 = -95.7 \pm 28.7$ kJ mol^{-1} and $\Delta s_T^0 = -26.5 \pm 28.7$ J mol^{-1} K^{-1}.

The results here are in reasonable agreement with the fitted value using the defect model. The difference in Δh_T^0 and Δs_T^0 may be attributed to the fact that ref 44 used $[Ce^{3+}]_{bulk} = 0.0071$ and for $[Ce^{3+}]_{surf} = 0.36$ for the calculation, while the results from our model are based on the entire data set. Nevertheless, the difference is within the error bar.

■ AUTHOR INFORMATION

Corresponding Authors
*(A.F.G.) E-mail: ghoniem@mit.edu. Tel.: +1 617-253-2295.
*(B.Y.) E-mail: byildiz@mit.edu. Tel.: +1 617-324-4009.

Notes
The authors declare no competing financial interest.

■ NOMENCLATURE

Symbols

a	lattice constant, m	
a_i	activity of species i	
C_i	species molar concentration, mol m^{-3}	
$\tilde{C}_i$	species molar concentration on the surface, mol m^{-2}	
D_i	diffusion coefficient, m^2 s^{-1}	
E	activation energy, kJ mol^{-1}	
F	Faraday constant	
f	difference between the measurements and the model predictions	
h	molar enthalpy, kJ mol^{-1}	
J_i	diffusion flux from the bulk phase, mol m^{-2}	

933	K_i	equilibrium constant
934	$k_{i,f}, k_{i,b}$	the rate coefficients for the forward and the backward reactions, s^{-1}
935	m	mass of sample, mg
936	$\dot{n}$	molar flow rate, mol s^{-1}
937	p_i	partial pressure of species i, bar
938	R	gas constant
939	$\dot{R}_i$	production/consumption rate of species i, mol m^{-2} s^{-1}
940	r_p	radius of ceria particle, m
941	r_i	reaction rate for reaction i, s^{-1}
942	S_R	surface area of the spherical particle, m^2
943	s_0, s_1	specific surface area of the fresh and aged samples, m^2 g^{-1}
944	s	molar enthalpy, J mol^{-1} K^{-1}
945	T	temperature, K
946	V_R	volume of the spherical particle, m^3
947	$\dot{V}$	volumetric flow rate, m^3 s^{-1}
948	X_i	species molar fraction
949 950	z_i	effective charge of species i

Greek Letters

952	γ_i	activity coefficient
953	$\Delta\delta$	bulk-phase nonstoichiometry change
954	$\tilde{\mu}_i$	electrochemical potential of species i, J mol^{-1}
955	$\tilde{\mu}_i^*$	electrochemical potential with the diffusion of the defect i, J mol^{-1}
956	$\tilde{\rho}_{Ce}$	molar density, mol m^{-3}
957	$\tilde{\rho}_{Ce,s}$	surface molar density, mol m^{-2}
958	ϕ	electrostatic potential, V
959 960	ω	measured splitting rate, μmol g^{-1}s^{-1}

Acronyms

962	OC	oxygen carrier
963	QMS	quadrupole mass spectrometer
964	RCLWS	reactive chemical-looping water splitting
965	SC	space-charge region
966	SMR	steam methane reforming
967 968	TCWS	thermochemical water splitting

■ REFERENCES

(1) Hosseini, S. E.; Wahid, M. A. Hydrogen Production from Renewable and Sustainable Energy Resources: Promising Green Energy Carrier for Clean Development. *Renewable Sustainable Energy Rev.* **2016**, *57*, 850−866.

(2) Lemus, R. G.; Martínez Duart, J. M. Updated Hydrogen Production Costs and Parities for Conventional and Renewable Technologies. *Int. J. Hydrogen Energy* **2010**, *35*, 3929−3936.

(3) Ramsden, T.; Ruth, M.; Diakov, V.; Laffen, M.; Timbario, T. *Hydrogen Pathways: Updated Cost, Well-to-Wheels Energy Use, and Emissions for the Current Technology Status of Ten Hydrogen Production, Delivery, and Distribution Scenarios*, Technical Report NREL/TP-6A10-60528; National Renewable Energy Laboratory (NREL): Golden, CO, USA, 2013.

(4) Siegel, N. P.; Miller, J. E.; Ermanoski, I.; Diver, R. B.; Stechel, E. B. Factors Affecting the Efficiency of Solar Driven Metal Oxide Thermochemical Cycles. *Ind. Eng. Chem. Res.* **2013**, *52*, 3276−3286.

(5) Steinfeld, A. Solar Thermochemical Production of Hydrogen−−a Review. *Sol. Energy* **2005**, *78*, 603−615.

(6) Chueh, W. C.; Falter, C.; Abbott, M.; Scipio, D.; Furler, P.; Haile, S. M.; Steinfeld, A. High-flux Solar-driven Thermochemical Dissociation of CO$_2$ and H$_2$O using Nonstoichiometric Ceria. *Science* **2010**, *330*, 1797−1801.

(7) Hao, Y.; Yang, C.-K.; Haile, S. M. High-temperature Isothermal Chemical Cycling for Solar-driven Fuel Production. *Phys. Chem. Chem. Phys.* **2013**, *15*, 17084−17092.

(8) McDaniel, A. H.; Miller, E. C.; Arifin, D.; Ambrosini, A.; Coker, E. N.; O'Hayre, R.; Chueh, W. C.; Tong, J. Sr-and Mn-doped

LaAlO$_{3-\delta}$ for Solar Thermochemical H$_2$ and CO Production. *Energy Environ. Sci.* **2013**, *6*, 2424−2428.

(9) Gokon, N.; Suda, T.; Kodama, T. Thermochemical Reactivity of 5−15 mol% Fe, Co, Ni, Mn-doped Cerium Oxides in Two-step Water-splitting Cycle for Solar Hydrogen Production. *Thermochim. Acta* **2015**, *617*, 179−190.

(10) Kaneko, H.; Miura, T.; Fuse, A.; Ishihara, H.; Taku, S.; Fukuzumi, H.; Naganuma, Y.; Tamaura, Y. Rotary-type Solar Reactor for Solar Hydrogen Production with Two-step Water Splitting Process. *Energy Fuels* **2007**, *21*, 2287−2293.

(11) Meng, Q.-L.; Lee, C.-i.; Kaneko, H.; Tamaura, Y. Solar Thermochemical Process for Hydrogen Production via Two-step Water Splitting Cycle Based on Ce$_{1-x}$Pr$_x$O$_{2-\delta}$ Redox Reaction. *Thermochim. Acta* **2012**, *532*, 134−138.

(12) Le Gal, A.; Abanades, S. Dopant Incorporation in Ceria for Enhanced Water-splitting Activity during Solar Thermochemical Hydrogen Generation. *J. Phys. Chem. C* **2012**, *116*, 13516−13523.

(13) Pappacena, A.; Boaro, M.; Armelao, L.; Llorca, J.; Trovarelli, A. Water Splitting Reaction on Ce$_{0.15}$Zr$_{0.85}$O$_2$ Driven by Surface Heterogeneity. *Catal. Sci. Technol.* **2016**, *6*, 399−403.

(14) Le Gal, A.; Abanades, S. Catalytic Investigation of Ceria-zirconia Solid Solutions for Solar Hydrogen Production. *Int. J. Hydrogen Energy* **2011**, *36*, 4739−4748.

(15) Le Gal, A.; Abanades, S.; Bion, N.; Le Mercier, T.; Harlé, V. Reactivity of Doped Ceria-Based Mixed Oxides for Solar Thermochemical Hydrogen Generation via Two-Step Water-Splitting Cycles. *Energy Fuels* **2013**, *27*, 6068−6078.

(16) Meng, Q.-L.; Lee, C.-i.; Ishihara, T.; Kaneko, H.; Tamaura, Y. Reactivity of CeO$_2$-based Ceramics for Solar Hydrogen Production via a Two-step Water-splitting Cycle with Concentrated Solar Energy. *Int. J. Hydrogen Energy* **2011**, *36*, 13435−13441.

(17) Kaneko, H.; Miura, T.; Ishihara, H.; Taku, S.; Yokoyama, T.; Nakajima, H.; Tamaura, Y. Reactive Ceramics of CeO$_2$−MO$_x$ (M= Mn, Fe, Ni, Cu) for H$_2$ Generation by Two-step Water Splitting Using Concentrated Solar Thermal Energy. *Energy* **2007**, *32*, 656−663.

(18) Lin, F.; Samson, V. A.; Wismer, A. O.; Grolimund, D.; Alxneit, I.; Wokaun, A. Zn-modified Ceria as a Redox Material for Thermochemical H$_2$O and CO$_2$ Splitting: Effect of a Secondary ZnO Phase on Its Thermochemical Activity. *CrystEngComm* **2016**, *18*, 2559−2569.

(19) Neises, M.; Roeb, M.; Schmücker, M.; Sattler, C.; Pitz-Paal, R. Kinetic Investigations of the Hydrogen Production Step of a Thermochemical Cycle Using Mixed Iron Oxides Coated on Ceramic Substrates. *Int. J. Energy Res.* **2010**, *34*, 651−661.

(20) Charvin, P.; Abanades, S.; Flamant, G.; Lemort, F. Two-step Water Splitting Thermochemical Cycle Based on Iron Oxide Redox Pair for Solar Hydrogen Production. *Energy* **2007**, *32*, 1124−1133.

(21) Demont, A.; Abanades, S.; Beche, E. Investigation of Perovskite Structures as Oxygen-Exchange Redox Materials for Hydrogen Production from Thermochemical Two-Step Water-Splitting Cycles. *J. Phys. Chem. C* **2014**, *118*, 12682−12692.

(22) Dey, S.; Naidu, B. S.; Govindaraj, A.; Rao, C. N. R. Noteworthy Performance of La$_{1-x}$Ca$_x$MnO$_3$ Perovskites in Generating H$_2$ and CO by the Thermochemical Splitting of H$_2$O and CO$_2$. *Phys. Chem. Chem. Phys.* **2015**, *17*, 122−125.

(23) Zhao, Z.; Chen, T.; Ghoniem, A. F. Rotary Bed Reactor for Chemical-Looping Combustion with Carbon Capture. Part 1: Reactor Design and Model Development. *Energy Fuels* **2013**, *27*, 327−343.

(24) Zhao, Z.; Iloeje, C. O.; Chen, T.; Ghoniem, A. F. Design of a Rotary Reactor for Chemical-Looping Combustion. Part 1: Fundamentals and Design Methodology. *Fuel* **2014**, *121*, 327−343.

(25) Zhao, Z.; Ghoniem, A. F. Design of a Rotary Reactor for Chemical-looping Combustion. Part 2: Comparison of Copper-, Nickel-, and Iron-based Oxygen Carriers. *Fuel* **2014**, *121*, 344−360.

(26) Zhao, Z.; Chen, T.; Ghoniem, A. F. Rotary Bed Reactor for Chemical-Looping Combustion with Carbon Capture. Part 2: Base Case and Sensitivity Analysis. *Energy Fuels* **2013**, *27*, 344−359.

(27) Iloeje, C.; Zhao, Z.; Ghoniem, A. F. Analysis of Thermally Coupled Chemical Looping Combustion-based Power Plants with Carbon Capture. *Int. J. Greenhouse Gas Control* **2015**, *35*, 56−70.

(28) Iloeje, C.; Zhao, Z.; Ghoniem, A. F. Efficient Cycles for Carbon Capture CLC Power Plants Based on Thermally Balanced Redox Reactors. *Int. J. Greenhouse Gas Control* **2015**, *41*, 302−315.

(29) Cho, W. C.; Seo, M. W.; Kim, S. D.; Kang, K. S.; Bae, K. K.; Kim, C. H.; Jeong, S. U.; Park, C. S. Reactivity of Iron Oxide as an Oxygen Carrier for Chemical-looping Hydrogen Production. *Int. J. Hydrogen Energy* **2012**, *37*, 16852−16863.

(30) Jin, G. T.; Ryu, H.-J.; Jo, S.-H.; Lee, S.-Y.; Son, S. R.; Kim, S. D. Hydrogen Production in Fluidized Bed by Chemical-looping Cycle. *Korean J. Chem. Eng.* **2007**, *24*, 542−546.

(31) Sun, S.; Zhao, M.; Cai, L.; Zhang, S.; Zeng, D.; Xiao, R. Performance of CeO_2-Modified Iron-Based Oxygen Carrier in the Chemical Looping Hydrogen Generation Process. *Energy Fuels* **2015**, *29*, 7612−7621.

(32) Chiron, F.-X.; Patience, G. S. Kinetics of Mixed Copper−iron Based Oxygen Carriers for Hydrogen Production by Chemical Looping Water Splitting. *Int. J. Hydrogen Energy* **2012**, *37*, 10526−10538.

(33) Son, S. R.; Go, K. S.; Kim, S. D. Thermogravimetric Analysis of Copper Oxide for Chemical-Looping Hydrogen Generation. *Ind. Eng. Chem. Res.* **2009**, *48*, 380−387.

(34) Kang, K.-S.; Kim, C.-H.; Cho, W.-C.; Bae, K.-K.; Woo, S.-W.; Park, C.-S. Reduction Characteristics of $CuFe_2O_4$ and Fe_3O_4 by Methane; $CuFe_2O_4$ as an Oxidant for Two-step Thermochemical Methane Reforming. *Int. J. Hydrogen Energy* **2008**, *33*, 4560−4568.

(35) Cha, K.-S.; Kim, H.-S.; Yoo, B.-K.; Lee, Y.-S.; Kang, K.-S.; Park, C.-S.; Kim, Y.-H. Reaction Characteristics of Two-step Methane Reforming over a Cu-ferrite/Ce−ZrO_2 Medium. *Int. J. Hydrogen Energy* **2009**, *34*, 1801−1808.

(36) Kang, K.-S.; Kim, C.-H.; Bae, K.-K.; Cho, W.-C.; Kim, W.-J.; Kim, Y.-H.; Kim, S.-H.; Park, C.-S. Redox Cycling of $CuFe_2O_4$ Supported on ZrO_2 and CeO_2 for Two-step Methane Reforming/Water Splitting. *Int. J. Hydrogen Energy* **2010**, *35*, 568−576.

(37) Kodama, T.; Shimizu, T.; Satoh, T.; Nakata, M.; Shimizu, K.-I. Stepwise Production of CO-rich Syngas and Hydrogen via Solar Methane Reforming by Using a Ni (II)−ferrite Redox System. *Sol. Energy* **2002**, *73*, 363−374.

(38) Sim, A.; Cant, N. W.; Trimm, D. L. Ceria−zirconia Stabilised Tungsten Oxides for the Production of Hydrogen by the Methane−water Redox Cycle. *Int. J. Hydrogen Energy* **2010**, *35*, 8953−8961.

(39) Otsuka, K.; Wang, Y.; Nakamura, M. Direct Conversion of Methane to Synthesis Gas through Gas−solid Reaction using CeO_2−ZrO_2 Solid Solution at Moderate Temperature. *Appl. Catal., A* **1999**, *183*, 317−324.

(40) Zhu, X.; Wang, H.; Wei, Y.; Li, K.; Cheng, X. Hydrogen and Syngas Production from Two-step Steam Reforming of Methane using CeO_2 as Oxygen Carrier. *J. Nat. Gas Chem.* **2011**, *20*, 281−286.

(41) Zhu, X.; Wang, H.; Wei, Y.; Li, K.; Cheng, X. Reaction Characteristics of Chemical-looping Steam Methane Reforming over a Ce−ZrO_2 Solid Solution Oxygen Carrier. *Mendeleev Commun.* **2011**, *21*, 221−223.

(42) Jeong, H. H.; Kwak, J. H.; Han, G. Y.; Yoon, K. J. Stepwise Production of Syngas and Hydrogen through Methane Reforming and Water Splitting by Using a Cerium Oxide Redox System. *Int. J. Hydrogen Energy* **2011**, *36*, 15221−15230.

(43) Zhu, X.; Wang, H.; Wei, Y.; Li, K.; Cheng, X. Hydrogen and Syngas Production from Two-step Steam Reforming of Methane over CeO_2-Fe_2O_3 Oxygen Carrier. *J. Rare Earths* **2010**, *28*, 907−913.

(44) Chueh, W. C.; McDaniel, A. H.; Grass, M. E.; Hao, Y.; Jabeen, N.; Liu, Z.; Haile, S. M.; McCarty, K. F.; Bluhm, H.; El Gabaly, F. Highly Enhanced Concentration and Stability of Reactive Ce_{3+} on Doped CeO_2 Surface Revealed In Operando. *Chem. Mater.* **2012**, *24*, 1876−1882.

(45) Feng, Z. A.; El Gabaly, F.; Ye, X.; Shen, Z.-X.; Chueh, W. C. Fast Vacancy-Mediated Oxygen Ion Incorporation across the Ceria−Gas Electrochemical Interface. *Nat. Commun.* **2014**, *5*, 4374.

(46) Trovarelli, A. Catalytic Properties of Ceria and CeO_2-containing Materials. *Catal. Rev.: Sci. Eng.* **1996**, *38*, 439−520.

(47) Mogensen, M.; Sammes, N. M.; Tompsett, G. A. Physical, Chemical and Electrochemical Properties of Pure and Doped Ceria. *Solid State Ionics* **2000**, *129*, 63−94.

(48) Panlener, R.; Blumenthal, R.; Garnier, J. A Thermodynamic Study of Nonstoichiometric Cerium Dioxide. *J. Phys. Chem. Solids* **1975**, *36*, 1213−1222.

(49) Tuller, H.; Nowick, A. Defect Structure and Electrical Properties of Nonstoichiometric CeO_2 Single Crystals. *J. Electrochem. Soc.* **1979**, *126*, 209−217.

(50) Paier, J.; Penschke, C.; Sauer, J. Oxygen Defects and Surface Chemistry of Ceria: Quantum Chemical Studies Compared to Experiment. *Chem. Rev.* **2013**, *113*, 3949−3985.

(51) Marrocchelli, D.; Yildiz, B. First-principles Assessment of H_2S and H_2O Reaction Mechanisms and the Subsequent Hydrogen Absorption on the CeO_2 (111) Surface. *J. Phys. Chem. C* **2012**, *116*, 2411−2424.

(52) Hansen, H. A.; Wolverton, C. Kinetics and Thermodynamics of H_2O Dissociation on Reduced CeO_2 (111). *J. Phys. Chem. C* **2014**, *118*, 27402−27414.

(53) Watkins, M. B.; Foster, A. S.; Shluger, A. L. Hydrogen Cycle on CeO_2 (111) Surfaces: Density Functional Theory Calculations. *J. Phys. Chem. C* **2007**, *111*, 15337−15341.

(54) Zhang, C.; et al. Measuring Fundamental Properties in Operating Solid Oxide Electrochemical Cells by Using in situ X-ray Photoelectron Spectroscopy. *Nat. Mater.* **2010**, *9*, 944−949.

(55) DeCaluwe, S. C.; Grass, M. E.; Zhang, C.; Gabaly, F. E.; Bluhm, H.; Liu, Z.; Jackson, G. S.; McDaniel, A. H.; McCarty, K. F.; Farrow, R. L.; Linne, M. A.; Hussain, Z.; Eichhorn, B. W. In Situ Characterization of Ceria Oxidation States in High-Temperature Electrochemical Cells with Ambient Pressure XPS. *J. Phys. Chem. C* **2010**, *114*, 19853−19861.

(56) Feng, Z. A.; Machala, M. L.; Chueh, W. C. Surface Electrochemistry of CO_2 Reduction and CO Oxidation on Sm-doped CeO_{2-x}: Coupling between Ce_{3+} and Carbonate Adsorbates. *Phys. Chem. Chem. Phys.* **2015**, *17*, 12273−12281.

(57) Ackermann, S.; Scheffe, J. R.; Steinfeld, A. Diffusion of Oxygen in Ceria at Elevated Temperatures and Its Application to H_2O/CO_2 Splitting Thermochemical Redox Cycles. *J. Phys. Chem. C* **2014**, *118*, 5216−5225.

(58) Al-Madfaa, H. A.; Khader, M. M. Reduction Kinetics of Ceria Surface by Hydrogen. *Mater. Chem. Phys.* **2004**, *86*, 180−188.

(59) Bulfin, B.; Lowe, A. J.; Keogh, K. A.; Murphy, B. E.; Lübben, O.; Krasnikov, S. A.; Shvets, I. V. Analytical Model of CeO_2 Oxidation and Reduction. *J. Phys. Chem. C* **2013**, *117*, 24129−24137.

(60) Knoblauch, N.; Dorrer, L.; Fielitz, P.; Schmucker, M.; Borchardt, G. Surface Controlled Reduction Kinetics of Nominally Undoped Polycrystalline CeO_2. *Phys. Chem. Chem. Phys.* **2015**, *17*, 5849−5860.

(61) Chen, T. Experimental Characterization and Chemical Kinetics Study of Chemical Looping Combustion, Master's Thesis; Massachusetts Institute of Technology: Cambridge, MA, USA, 2014.

(62) Maier, J. *Physical Chemistry of Ionic Materials: Ions and Electrons in Solids*; John Wiley & Sons: Chichester, U.K., 2004.

(63) Stan, M.; Zhu, Y. T.; Jiang, H.; Butt, D. P. Kinetics of Oxygen Removal from Ceria. *J. Appl. Phys.* **2004**, *95*, 3358−3361.

(64) Lagarias, J. C.; Reeds, J. A.; Wright, M. H.; Wright, P. E. Convergence Properties of the Nelder-Mead Simplex Method in Low Dimensions. *SIAM Journal on optimization* **1998**, *9*, 112−147.